coatings

MDPI

Article

Mixed Convection Flow of Magnetized Casson Nanofluid over a Cylindrical Surface

Firas A. Alwawi [1,2], Abdulkareem Saleh Hamarsheh [1,*], Hamzeh T. Alkasasbeh [3] and Ruwaidiah Idris [2]

[1] Department of Mathematics, College of Sciences and Humanities in Al-Kharj, Prince Sattam Bin Abdulaziz University, Al-Kharj 11942, Saudi Arabia; f.alwawi@psau.edu.sa
[2] Special Interest Group of Modelling and Data Analytics (SIGMDA), Faculty of Ocean Engineering Technology and Informatics, Universiti Malaysia Terengganu, Kuala Nerus 21030, Terengganu, Malaysia; ruwaidiah@umt.edu.my
[3] Department of Mathematics, Faculty of Science, Ajloun National University, Ajloun 26810, Jordan; alkasasbehh@gmail.com
* Correspondence: a.hamarsheh@psau.edu.sa

Abstract: This work aimed to establish a numerical simulation of kerosene oil as a host Casson fluid flowing around a cylindrical shape with an applied magnetic field crossing through it, under constant wall temperature boundary conditions. Nanoparticles of zinc, aluminum, and titanium oxides were included to reinforce its thermal characteristics. The governing model was established based on the Tiwari and Das model. Graphical and numerical results for correlated physical quantities were gained through the Keller Box method, with the assistance of MATLAB software (9.2). The combined convection ($\lambda > 0$ & $\lambda < 0$), magnetic parameter ($M > 0$), Casson parameter ($\beta > 0$), and nanosolid volume fraction ($0.1 \leq \chi \leq 0.2$) were the parameter ranges considered in this study. According to the current findings, the growth of mixed convection parameter or volume fraction of ultrafine particles contributes to boosting the rate of energy transport, skin friction, and velocity distribution. Zinc oxide–kerosene oil has the highest velocity and temperature, whatever the parameters influencing it.

Keywords: casson nanofluid; cylindrical shape; kerosene oil; MHD; combined convection

check for updates

Citation: Alwawi, F.A.; Hamarsheh, A.S.; Alkasasbeh, H.T.; Idris, R. Mixed Convection Flow of Magnetized Casson Nanofluid over a Cylindrical Surface. *Coatings* **2022**, *12*, 296. https://doi.org/10.3390/coatings12030296

Academic Editors: Yujun Song and George Kokkoris

Received: 6 December 2021
Accepted: 19 February 2022
Published: 22 February 2022
Corrected: 10 February 2026

Publisher's Note: MDPI stays neutral with regard to jurisdictional claims in published maps and institutional affiliations.

Copyright: © 2022 by the authors. Licensee MDPI, Basel, Switzerland. This article is an open access article distributed under the terms and conditions of the Creative Commons Attribution (CC BY) license (https://creativecommons.org/licenses/by/4.0/).

1. Introduction

A Casson liquid is indeed a non-Newtonian liquid that behaves similarly to an elastic material in which no motion occurs with a low yield stress (see [1]). It's suitable for heating or cooling operations due to its efficient impact on the energy transmission rate, giving it eligibility for utilization in many applications relevant to food processing, metallurgy, drilling, and bioengineering operations. Casson [2] was the first to address the Casson fluid model (rheological model). He demonstrated in his study that the Casson model is effective in modeling the flow of pigment suspensions in lithographic polishes employed during the production of printing ink. The Casson model is also capable of effectively describing the flow characteristics of numerous polymers widely [3]. Furthermore, experiments conducted on blood have shown that blood can act as a Cassone fluid, especially when the shear stress is low, and the flow occurs through small blood vessels [4–6]. Human blood, honey, jelly, tomato sauce, custard, toothpaste, starch suspensions, foams, molten cosmetics, yogurt, and nail polish are familiar examples of this fluid. In view of the high efficiency of the Casson model in predicting the behavior of non-Newtonian fluids, several studies have recently been conducted that relied on the Casson model. Mustafa et al. [7] reported that the velocity is a decreasing function of dimensionless time but that temperature is an increasing function of it, and that raising the Casson parameter boosts shear stress and heat transfer. Mukhopadhyay et al. [8] utilized the shooting method to examine the Casson liquid flow and energy transmission on a stretching surface. Khalid et al. [9] addressed the magneto-free convection of a Casson liquid from an oscillating vertical plate in a porous medium.

Animasaun et al. [10] demonstrated that growth in the values of the Casson parameter causes velocity curve augmentation and temperature curve reduction. EL-Kabeir et al. [11] investigated the effect of chemical reactions on the mixed convection flow of Casson liquid over a sphere. Makinde et al. [12] revealed that there is a critical relationship between the impact of the Lorentz force and the flow of Casson fluid, with the natural impact of this force occurring when the surface thickness is low, and the exact opposite of this influence occurring when the surface thickness increases. In their examination of the magneto-3D flow of non-Newtonian Casson liquid with thermal radiation, Thumma et al. [13] observed that raising the Casson parameter values considerably reduces the velocity curve. For more reading, see the following articles [14–17].

A notable number of thermal applications in industrial and engineering are extensively dependent on convection through regular fluids. Therefore, the challenge for researchers was how to enhance the energy transport rate by several methods. One of these creative methods is addressed by Choi and Eastman [18]. They proposed that suspending copper nanoparticles in regular fluids leads to an improvement in their thermophysical properties. Subsequently, Eastman et al. [19] confirmed that there is a considerable effect of the shape and volume fraction of Cu nanoparticles that are immersed in ethylene glycol on the thermal conductivity. Choi and Eastman's suggestion sparked a new challenge, which was to find an ideal nanoparticle that would produce the maximum improvement in the rate of heat transfer while maintaining the lowest possible density of the nanoliquid, considering other aspects that could not be ignored, such as stability, cost, waste management ability, etc. Several experimental studies have confirmed that metal oxides are almost ideal for enhancing the rate of energy transfer of ordinary liquids. They have been widely synthesized during the last few decades and used in a variety of applications. Among them are included the ultrafine particles of zinc, aluminum, and titanium oxides (ZnO, Al_2O_3, TiO_2). They were investigated experimentally in a variety of energy systems, including heat exchangers, cooling, pool boiling, and transformer systems [20–26], in addition to extensive numerical simulation studies demonstrating the efficacy of these oxides in promoting heat transfer [27–34].

Kerosene oil (KO) is a combustible hydrocarbon liquid that is extracted from petroleum. It is extensively utilized as jet fuel and in some rocket engines, and is additionally employed as a cooking and lighting fuel. In some regions of Asia, it is also used to power small outboard motors or even motorcycles. In the field of energy transmission, kerosene is mainly used in regenerative cooling techniques, as it is used to cool nozzles and chambers in rocket engines [35]. Many researchers have considered kerosene oil as a base liquid in their work, in addition to enhancing its thermal properties by incorporating nanoparticles. Hussain et al. [36] reported the natural convection flow of kerosene and engine oil-based micropolar nanofluid. Ellahi et al. [37] demonstrated that a nanofluid containing Al_2O_3 and kerosene oil can improve chamber and nozzle cooling. Other interesting studies regarding kerosene oil in the field of heat transfer can be found in the refs. [38–42]. In order to conduct a useful and comprehensive examination, kerosene oil was adopted as the host liquid in this work due to its unusual thermophysical properties, such as viscosity, heat capacity, thermal conductivity, density, etc.

Flowing fluid around a circular cylinder in the boundary layer region is a key subject in many industrial and mechanical operations, such as venomous fluid motion, film condensation operation of a liquid, manufacturing, and extracting plates of caoutchouc, etc. Magnetohydrodynamics (MHD) has also played a critical part in a variety of current metallurgy and metalworking industries, as well as numerous natural phenomena. Qasim et al. [43] examined the convection slip flow of ferrofluid past a stretching cylinder under an MHD effect. Tamoor et al. [44] analyzed the convection of Casson liquid with Joule heating and MHD effects over a stretching cylinder. Alizadeh et al. [45] examined the impact of radiation on combined convection flow, considering the magnetic force on a cylinder in a porous medium. Krishna [46] studied the MHD convective rotating flow of second grade

liquid past a heat generating vertical moving permeable surface with hall and ion slip effects. Here are some related and important recent studies [47–55].

In 2006, Buongiorno [56] constructed a mathematical model that demonstrates the significance of Brownian diffusion and thermophoresis in heat transmission via nanofluids, whereas Tiwari and Das [57] highlighted the influence of nanoparticle volume fraction on energy transmission in their single-phase model in 2007. Since then, these two models have been the most commonly employed in predicting the behavior of nanofluids in heat transfer-related issues. Constant wall temperature boundary conditions are widely used in a variety of industrial processes, particularly in heat exchange applications such as condensing vapors or boiling liquids. Also, in applications in which the energy transport coefficient of the outer surface is greater than the inner surface, a constant wall temperature can be taken into account. See [58–61] for details.

In this analysis, Tiwari and Das's model was adopted to provide insight into the impact of critical parameters on physical quantities concerning energy transfer in the presence of an imposed magnetic field, considering the combined convection case of flowing kerosene oil-based Casson fluid around a circular cylinder under constant wall temperature. In particular, it provides answers about the extent of influence parameters of mixed convection, magnetic, Casson, and the volume fraction of ultrafine particles, as well as their interaction with each other. Furthermore, this work is seen as an extension and improvement of some previous investigations noted below that are related to fluid flow around a cylinder in the boundary layer region. Merkin [62,63] examined the flow of a fluid in free and mixed convection. Nazar et al. [64,65] illustrated the combination of free and forced convection flow of micropolar fluid subjected to two different boundary conditions. Tham et al. [66] examined the combined convection flow of nanoliquid. Rashad et al. [67] analyzed the combined convection of nanofluid in a porous medium. Alwawi et al. [68] reported the enhancement of the energy transfer of methanol as a host Casson fluid with the effect of MHD.

2. Modeling of the Problem

Suppose we have a kerosene oil flow containing suspensions of Al_2O_3, ZnO, and TiO_2 nanoparticles in the presence of combined convection around a circular cylinder of radius a under the impact of Lorentz force, with a constant wall temperature T_w, in addition to the surrounding temperature T_∞. Also, a heated and cooled circular cylinder ($T_w > T_\infty$ and $T_w < T_\infty$, respectively) are taken into account. Figure 1 displays the flow layout and the schematic diagram, where U_∞ indicates free stream velocity, and g stands for heat gravity vector. The $\hat{x}$-coordinate will be measured along the circumference of the circular cylinder at the point of stagnation ($\hat{x} \approx 0$), while the $\hat{y}$-coordinates will be the normal distance to the circular cylinder surface.

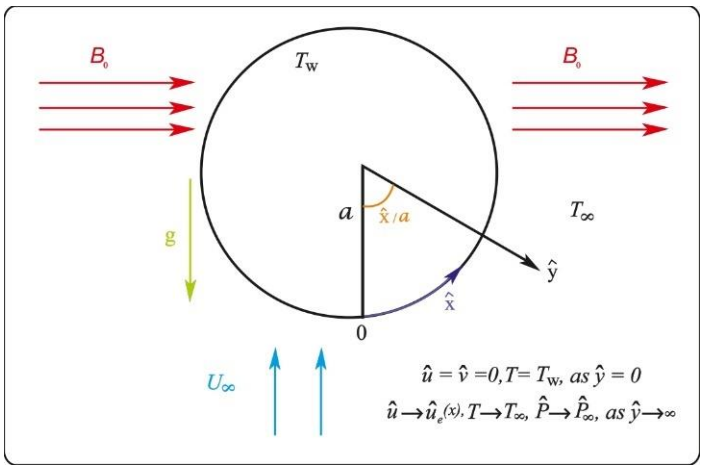


Figure 1. Layout and geometrical coordinates flow.

Hussanan et al. [69] described the Casson liquid flow as:

$$\tau_{ij} = \begin{cases} 2\left(\mu_B + p_y/\sqrt{2\pi}\right)e_{ij} & \pi > \pi_c, \\ 2\left(\mu_B + p_y/\sqrt{2\pi_c}\right)e_{ij} & \pi < \pi_c, \end{cases} \tag{1}$$

Using the previously stated assumptions, the Boussinesq approximation [70], and boundary layers approximation [71], the governing system is (see [14,15,69,72,73]):

$$\frac{\partial \hat{u}}{\partial \hat{x}} + \frac{\partial \hat{v}}{\partial \hat{y}} = 0, \tag{2}$$

$$\begin{aligned} \hat{u}\frac{\partial \hat{u}}{\partial \hat{x}} + \hat{v}\frac{\partial \hat{u}}{\partial \hat{y}} = & -\frac{1}{\rho_{nf}}\frac{\partial \widetilde{P}}{\partial \widetilde{\xi}} + v_{nf}\left(1+\frac{1}{\beta}\right)\frac{\partial^2 \hat{u}}{\partial \hat{y}^2} \\ & + \left(\frac{\chi\rho_s\beta_s + (1-\chi)\rho_f\beta_f}{\rho_{nf}}\right)g(T-T_\infty)\sin\left(\frac{\hat{x}}{a}\right) - \frac{\delta_{nf}B_0^2}{\rho_{nf}}\hat{u}, \end{aligned} \tag{3}$$

$$\hat{u}\frac{\partial T}{\partial \hat{x}} + \hat{v}\frac{\partial T}{\partial \hat{y}} = \alpha_{nf}\frac{\partial^2 T}{\partial \hat{y}^2}, \tag{4}$$

Subject to (see [66]):

$$\begin{aligned} \hat{u} = \hat{v} = 0, T = T_w, \ as \ \hat{y} = 0 \\ \hat{u} \to \hat{u}_e(x), T \to T_\infty, \ \hat{P} \to P_\infty \ as \ \hat{y} \to \infty, \end{aligned} \tag{5}$$

The properties of nanofluid are (defined by [74]):

$$\begin{aligned} &\frac{\sigma_{nf}}{\sigma_f} = 1 + \frac{3(\sigma-1)\chi}{(\sigma+2)-(\sigma-1)\chi}, \ \sigma = \frac{\sigma_s}{\sigma_f}, \ \mu_{nf} = \frac{\mu_f}{(1-\chi)^{2.5}}, \ \rho_{nf} = (1-\chi)\rho_f + \chi\rho_s, \\ &(\rho c_p)_{nf} = (1-\chi)(\rho c_p)_f + \chi(\rho c_p)_s, \ \frac{k_{nf}}{k_f} = \frac{(k_s+2k_f)-2\chi(k_f-k_s)}{(k_s+2k_f)+\chi(k_f-k_s)}, \ \alpha_{nf} = \frac{k_{nf}}{(\rho c_p)_{nf}}, \end{aligned} \tag{6}$$

The following variables are employed for non-dimensionalization (see [66]):

$$\begin{aligned} x = \frac{\hat{x}}{a}, y = \mathrm{Re}^{1/2}\left(\frac{\hat{y}}{a}\right), u = \frac{\hat{u}}{U_\infty}, \ \theta = \frac{T-T_\infty}{T_w-T_\infty} \\ v = \mathrm{Re}^{1/2}\left(\frac{\hat{v}}{U_\infty}\right), u_e(x) = \frac{\hat{u}_e(\hat{x})}{U_\infty}, \ \hat{u}_e(\hat{x}) = U_\infty \sin\left(\frac{\hat{x}}{a}\right) \end{aligned} \tag{7}$$

where $\mathrm{Re} = U_\infty a/v_f$ is the Reynolds number.

Using Equation (7) yields the dimensionless equations shown below.

$$\frac{\partial u}{\partial x} + \frac{\partial v}{\partial y} = 0. \tag{8}$$

$$\begin{aligned} u\frac{\partial u}{\partial x} + v\frac{\partial u}{\partial y} = & -\frac{\partial p}{\partial \xi} + \frac{\rho_f}{\rho_{nf}}\frac{1}{(1-\chi)^{2.5}}\left(1+\frac{1}{\beta}\right)\frac{\partial^2 u}{\partial y^2} \\ & + \left(\frac{\chi\rho_s\beta_s/\beta_f + (1-\chi)\rho_f}{\rho_{nf}}\right)\lambda\theta\sin x - \frac{\sigma_{nf}B_0^2 a}{\rho_{nf}U_\infty}u, \end{aligned} \tag{9}$$

$$u\frac{\partial \theta}{\partial x} + v\frac{\partial \theta}{\partial y} = \frac{1}{\mathrm{Pr}}\left(\frac{k_{nf}/k_f}{(1-\chi)+\chi(\rho c_p)_s/(\rho c_p)_f}\right)\frac{\partial^2 \theta}{\partial y^2}, \tag{10}$$

Subject to:

$$u = v = 0, \ \theta = 1 \ as \ y = 0, u \to u_e(x), \ \theta \to 0 \ as \ y \to \infty. \tag{11}$$

where $\lambda = \frac{Gr}{\mathrm{Re}^2}$, $Gr = g\beta_f(T_w - T_\infty)\frac{a^3}{v_f^2}$,, and $\mathrm{Pr} = \frac{v_f}{\alpha_f}$ are the mixed convection parameter, and Grashof and Prandtl numbers, respectively.

By using the nondimensional form of generalized Bernoulli's equation, which is given by Dinarvand et al. [75] as follows:

$$u_e \frac{\partial u_e}{\partial \widetilde{\xi}} = -\left(\frac{\partial P}{\partial \xi} + \frac{\sigma_{nf} B_0^2 a}{\rho_{nf} U_\infty} u_e \right) \tag{12}$$

Equation (9) becomes:

$$\begin{aligned} u\frac{\partial u}{\partial x} + v\frac{\partial u}{\partial y} = \quad & u_e \frac{du_e}{\partial x} + \frac{\rho_f}{\rho_{nf}} \frac{1}{(1-\chi)^{2.5}} \left(1 + \frac{1}{\beta}\right) \frac{\partial^2 u}{\partial y^2} \\ & + \left(\frac{\chi \rho_s \beta_s / \beta_f + (1-\chi)\rho_f}{\rho_{nf}} \right) \lambda \theta \sin x + \frac{\rho_f \delta_{nf}}{\rho_{nf} \delta_f} M(u_e - u), \end{aligned} \tag{13}$$

where $M = \left(\frac{\sigma_f \beta_0^2 a}{\rho_f U_\infty} \right)$ is the magnetic parameter.

To reduce the previous system, we'll introduce the following transformation (given by [14]):

$$\psi = xF(x,y),\ \theta = \theta(x,y), \tag{14}$$

where ψ is the stream function, defined as:

$$u = \frac{\partial \psi}{\partial y}, \text{ and } v = -\frac{\partial \psi}{\partial x}$$

Applying the transformation (14), the non-dimensional system turns into:

$$\begin{aligned} & \frac{\rho_f}{\rho_{nf}} \frac{1}{(1-\chi)^{2.5}} \left(1 + \frac{1}{\beta}\right) \frac{\partial^3 F}{\partial y^3} + F\frac{\partial^2 F}{\partial y^2} - \left(\frac{\partial F}{\partial y}\right)^2 + \frac{\rho_f \delta_{nf}}{\rho_{nf} \delta_f} M \left(\frac{\sin x}{x} - \frac{\partial F}{\partial y}\right) \\ & + \frac{\sin x \cos x}{x} + \left(\frac{\chi \rho_s \beta_s / \beta_f + (1-\chi)\rho_f}{\rho_{nf}} \right) \lambda \theta \frac{\sin x}{x} = x\left(\frac{\partial F}{\partial y}\frac{\partial^2 F}{\partial x \partial y} - \frac{\partial F}{\partial x}\frac{\partial^2 F}{\partial y^2} \right), \end{aligned} \tag{15}$$

$$\frac{1}{\mathrm{Pr}} \left(\frac{k_{nf}/k_f}{(1-\chi) + \chi \left(\rho c_p\right)_s / \left(\rho c_p\right)_f} \right) \frac{\partial^2 \theta}{\partial y^2} + F\frac{\partial \theta}{\partial y} = x\left(\frac{\partial F}{\partial y}\frac{\partial \theta}{\partial x} - \frac{\partial F}{\partial x}\frac{\partial \theta}{\partial y} \right), \tag{16}$$

and boundary conditions (11) become:

$$\begin{aligned} & \frac{\partial F}{\partial y} = F = 0,\ \theta = 1,\ \text{as } y = 0, \\ & \frac{\partial F}{\partial y} \to \frac{\sin x}{x},\ \theta \to 0 \text{ as } y \to \infty, \end{aligned} \tag{17}$$

The system (15)–(17) converts to the following ODEs at the lower stagnation point of the cylinder $(x \approx 0)$,

$$\begin{aligned} \frac{\rho_f}{\rho_{nf}} \frac{1}{(1-\chi)^{2.5}} \quad & \left(1 + \frac{1}{\beta}\right) F''' + FF'' - (F')^2 \\ & + \left(\frac{\chi \rho_s \beta_s / \beta_f + (1-\chi)\rho_f}{\rho_{nf}} \right) \lambda \theta + \frac{\rho_f \delta_{nf}}{\rho_{nf} \delta_f} M\,(1 - F') + 1 = 0, \end{aligned} \tag{18}$$

$$\frac{1}{\mathrm{Pr}} \left(\frac{k_{nf}/k_f}{(1-\chi) + \chi \left(\rho c_p\right)_s / \left(\rho c_p\right)_f} \right) \theta'' + F\theta' = 0, \tag{19}$$

$$\begin{aligned} & F' = F = 0,\ \theta = 1\ as\ y = 0 \\ & F' \to 1,\ \theta \to 0\ as\ y \to \infty \end{aligned} \tag{20}$$

The most effective non-dimensional quantity for depicting shear stress is the skin friction coefficient C_f. It reflects the total frictional drag acting on an object and is directly related to the heat transfer rate through convection on a surface. The skin friction coefficient increase is considered a disadvantage in some technical applications. Besides that, the Nusselt number Nu is a non-dimensional characteristic group that describes the ratio of energy transmission via convection to energy transmission via conduction within the fluid.

It is a key parameter in determining the mode of energy transfer and a non-dimensional characteristic number for the energy transport rate. The small value of the Nusselt number indicates that the energy transfer through convection almost does not exist, and the energy transfer completely occurs through the conduction process, whereas the higher values of the Nusselt number mean that the opposite entirely occurs and most of the energy is transferred by the convection process. Molla et al. [76] expressed skin friction and the local Nusselt number as follows:

$$C_f = \left(\frac{\tau_w}{\rho U_\infty^2}\right), \; Nu = \left(\frac{a q_w}{k_f (T_w - T_\infty)}\right), \tag{21}$$

where

$$\tau_w = \mu_{nf}\left(1 + \frac{1}{\beta}\right)\left(\frac{\partial \hat{u}}{\partial \hat{y}}\right)_{\hat{y}=0}, \; q_w = -k_{nf}\left(\frac{\partial T}{\partial \widetilde{\eta}}\right)_{\hat{y}=0}. \tag{22}$$

Applying (7) and (11), C_f and Nu can be rewritten as follows:

$$\mathrm{Re}^{1/2} C_f = \frac{1}{(1-\chi)^{2.5}}\left(1 + \frac{1}{\beta}\right) x \left(\frac{\partial^2 F}{\partial y^2}\right)_{y=0}, \; \mathrm{Re}^{-1/2} Nu = \frac{-k_{nf}}{k_f}\left(\frac{\partial \theta}{\partial y}\right)_{y=0} \tag{23}$$

3. Numerical Solution

A technique called the Keller box technique was introduced by Keller and Bramble [77] in 1970. It gained popularity when Jones [78] employed it to tackle boundary layer-related issues. In their book, Cebeci and Bradshaw [79] provided an extensive explanation of this method. This approach is one of the most important strategies for solving parabolic flow equations, particularly boundary layer equations. These schemes are implicit in second-order precision in both space and time, and they allow for arbitrary step sizes in both time and space (nonuniform). This makes it useful and efficient for solving parabolic partial differential equations. Equations (15) and (16) are recast at the start of this approach to produce first-order equations. The difference equations are then found using the central differences approach. The resulting equations are then linearized utilizing Newton's technique. The matrix–vector form is then written. Finally, a tridiagonal matrix is generated, and the linear system is solved using LU factorization.

3.1. The Finite Difference Technique

Equations (15) and (16) are converted into first-order equations using the following transformation: $O(x, y)$, $Q(x, y)$, $I(x, y)$, and $H(x, y)$, where the variable $T(x, y)$ was used instead of the temperature variable $\theta(x, y)$, and

$$\begin{aligned} F' &= O \\ O' &= Q \\ H' &= I \end{aligned} \tag{24}$$

Consequently, Equations (15) and (16) turn into:

$$\begin{aligned} &\frac{\rho_f}{\rho_{nf}} \frac{1}{(1-\chi)^{2.5}}\left(1 + \frac{1}{\beta}\right) Q' + FQ - O^2 + \frac{\rho_f \sigma_{nf}}{\rho_{nf} \sigma_f} M \left(\frac{\sin x}{x} - O\right) \\ &+ \left(\frac{\chi \rho_s \beta_s / \beta_f + (1-\chi)\rho_f}{\rho_{nf}}\right) \lambda T \frac{\sin x}{x} + \frac{\sin x \cos x}{x} = x\left(O\frac{\partial O}{\partial x} - Q\frac{\partial F}{\partial x}\right), \end{aligned} \tag{25}$$

$$\frac{1}{\mathrm{Pr}}\left(\frac{k_{nf}/k_f}{(1-\chi) + \chi\left(\rho c_p\right)_s / \left(\rho c_p\right)_f}\right) I' + FI' = x\left(O\frac{\partial H}{\partial x} - I\frac{\partial F}{\partial x}\right), \tag{26}$$

Subject to:

$$\begin{aligned} O(x,0) &= F(x,0) = 0, \; H(x,0) = 1, \\ O(x,\infty) &= \frac{\sin x}{x}, \; H(x,\infty) = 0, \end{aligned} \tag{27}$$

Here, the symbol prime indicates the first derivative with respect to x.

Now center Equation (24) about the midpoint $(x^{\,n}, y_{j-1/2})$ of the segment and center Equations (25) and (26) about the midpoint. $(x^{n-1/2}, y_{j-1/2})$ of the rectangle as follows:

$$F_j^n - F_{j-1}^n - \frac{h_j}{2}\left(O_j^n + O_{j-1}^n\right) = 0. \tag{28}$$

$$O_j^n - O_{j-1}^n - \frac{h_j}{2}\left(Q_j^n + Q_{j-1}^n\right) = 0. \tag{29}$$

$$H_j^n - H_{j-1}^n - \frac{h_j}{2}\left(I_j^n + I_{j-1}^n\right) = 0. \tag{30}$$

$$\begin{aligned}
&\tfrac{\rho_f}{\rho_{nf}}\tfrac{1}{(1-\chi)^{2.5}}\left(1+\tfrac{1}{\beta}\right)\left(Q_j^n - Q_{j-1}^n\right) + \left(\tfrac{1+\alpha}{4}\right)h_j(F_j^n + F_{j-1}^n)(Q_j^n + Q_{j-1}^n)\\
&\quad -\left(\tfrac{1+\alpha}{4}\right)h_j\,(O_j^n + O_{j-1}^n)^2 + \left(\tfrac{\alpha}{2}\right)h_j Q_{j-1/2}^{n-1}(F_j^n + F_{j-1}^n)\\
&\quad +\tfrac{1}{2}\left(\frac{\chi\rho_s\left(\beta_s/\beta_f\right)+(1-\chi)\rho_f}{\rho_{nf}}\right)\tfrac{\sin x^{n-1/2}}{x^{n-1/2}}\lambda h_j(H_j^n + H_{j-1}^n)\\
&\quad +\tfrac{\rho_f\delta_{nf}}{\rho_{nf}\delta_f}Mh_j(\tfrac{\sin x^{n-1/2}}{x^{n-1/2}} - \tfrac{O_j^n + O_{j-1}^n}{2}) - \left(\tfrac{\alpha}{2}\right)h_j F_{j-1/2}^{n-1}(Q_j^n + Q_{j-1}^n)\\
&\quad +\tfrac{\sin x^{n-1/2}\cos x^{n-1/2}}{x^{n-1/2}}h_j = (R_1)_{j-1/2}^{n-1}
\end{aligned} \tag{31}$$

$$\begin{aligned}
&\tfrac{1}{\mathrm{Pr}}\frac{k_{nf}/k_f}{\left((1-\chi)(\rho C_p)_f + \chi\left(\rho c_p\right)_s/\left(\rho c_p\right)_f\right)}\left(I_j^n - I_{j-1}^n\right)\\
&\quad -\tfrac{\alpha}{4}h_j(O_j^n + O_{j-1}^n)(H_j^n + H_{j-1}^n) + \tfrac{1+\alpha}{4}h_j(F_j^n + F_{j-1}^n)(I_j^n + I_{j-1}^n)\\
&\quad +\tfrac{\alpha}{2}h_j(O_j^n + O_{j-1}^n)H_{j-1/2}^{n-1} - \tfrac{\alpha}{2}h_j O_{j-1/2}^{n-1}(H_j^n + H_{j-1}^n) - \tfrac{\alpha}{2}h_j(I_j^n - I_{j-1}^n)F_{j-1/2}^{n-1}\\
&\quad +\tfrac{\alpha}{2}h_j I_{j-1/2}^{n-1}(F_j^n + F_{j-1}^n) = (R_2)_{j-1/2}^{n-1}
\end{aligned} \tag{32}$$

where $\alpha = \frac{x^{n-1/2}}{k_n}$, $k_n is\ \Delta x$, and $h_j\ is\ \Delta y$

$$(R_1)_{j-1/2}^{n-1} = -h_j\left(\begin{array}{l}
\tfrac{\rho_f}{\rho_{nf}}\tfrac{1}{(1-\chi)^{2.5}}\left(1+\tfrac{1}{\beta}\right)\tfrac{\left(Q_j^n - Q_{j-1}^n\right)}{h_j} + (1-\alpha)F_{j-1/2}^n Q_{j-1/2}^n\\
+(\alpha-1)\left(O_{j-1/2}^n\right)^2 + \tfrac{\rho_f\sigma_{nf}}{\rho_{nf}\sigma_f}M(\tfrac{\sin x^{n-1/2}}{x^{n-1/2}} - O_{j-1/2}^n) + \tfrac{\sin x^{n-1/2}\cos x^{n-1/2}}{x^{n-1/2}}\\
\quad +\left(\frac{\chi\rho_s\left(\beta_s/\beta_f\right)+(1-\chi)\rho_f}{\rho_{nf}}\right)\tfrac{\sin x^{n-1/2}}{x^{n-1/2}}\lambda H_{j-1/2}^n
\end{array}\right)^{n-1}$$

$$(R_1)_{j-1/2}^{n-1} = -h_j\left(\begin{array}{l}
\tfrac{\rho_f}{\rho_{nf}}\tfrac{1}{(1-\chi)^{2.5}}\left(1+\tfrac{1}{\beta}\right)\tfrac{\left(Q_j^n - Q_{j-1}^n\right)}{h_j} + (1-\alpha)F_{j-1/2}^n Q_{j-1/2}^n\\
+(\alpha-1)\left(O_{j-1/2}^n\right)^2 + \tfrac{\rho_f\sigma_{nf}}{\rho_{nf}\sigma_f}M(\tfrac{\sin x^{n-1/2}}{x^{n-1/2}} - O_{j-1/2}^n) + \tfrac{\sin x^{n-1/2}\cos x^{n-1/2}}{x^{n-1/2}}\\
\quad +\left(\frac{\chi\rho_s\left(\beta_s/\beta_f\right)+(1-\chi)\rho_f}{\rho_{nf}}\right)\tfrac{\sin x^{n-1/2}}{x^{n-1/2}}\lambda H_{j-1/2}^n
\end{array}\right)^{n-1} \tag{33}$$

At $x = x^n$, the boundary conditions are:

$$\begin{aligned}
F_0^n &= O_0^n = 0,\ H_0^n = 1,\\
O_J^n &= \tfrac{\sin x}{x},\ H_J^n = 0\,,
\end{aligned} \tag{34}$$

3.2. Newton's Method

By applying Newton's technique to the system (28)–(32), we get:

$$\delta F_j - \delta F_{j-1} - \frac{1}{2}h_j\left(\delta O_j + \delta O_{j-1}\right) = (r_1)_{j-1/2} \tag{35}$$

$$\delta O_j - \delta O_{j-1} - \frac{1}{2}h_j\left(\delta Q_j + \delta Q_{j-1}\right) = (r_2)_{j-1/2} \tag{36}$$

$$\delta H_j - \delta H_{j-1} - \frac{1}{2}h_j\Big(\delta I_j + \delta I_{j-1}\Big) = (r_3)_{j-1/2} \tag{37}$$

$$\begin{aligned}(m_1)_j\delta Q_j + (m_2)_j\delta Q_{j-1} + (m_3)_j\delta F_j + (m_4)_j\delta F_{j-1} + (m_5)_j\delta O_j \\ +(m_6)_j\delta O_{j-1} + (m_7)_j\delta H_j + (m_8)_j\delta H_{j-1} = \ (r_4)_{j-1/2}\end{aligned} \tag{38}$$

$$\begin{aligned}\big(n_1\big)_j\delta I_j + (n_2)_j\delta I_{j-1} + (n_3)_j\delta F_j + \big(n_4\big)_j\delta F_{j-1} + (n_5)_j\delta O_j \\ +(n_6)_j\delta O_{j-1} + (n_7)_j\delta H_j + (n_8)_j\delta H_{j-1} \ = (r_5)_{j-1/2}\end{aligned} \tag{39}$$

where

$$\begin{aligned}(m_1)_j &= \left[\frac{\rho_f}{\rho_{nf}}\frac{1}{(1-\chi)^{2.5}}\Big(1+\tfrac{1}{\beta}\Big) + h_j\left(\tfrac{(1+\alpha)}{2}F_{j-1/2} - \tfrac{\alpha}{2}F^{n-1}_{j-1/2}\right)\right]\\
(m_2)_j &= \left[(m_1)_j \ - \ 2\frac{\rho_f}{\rho_{nf}}\frac{1}{(1-\chi)^{2.5}}\Big(1+\tfrac{1}{\beta}\Big)\right]\\
(m_3)_j &= h_j\Big[\tfrac{(1+\alpha)}{2}z_{j-1/2} + \tfrac{\alpha}{2}Q^{n-1}_{j-1/2}\Big]\\
(m_4)_j &= (m_3)_j\\
(m_5)_j &= \ h_j\Big[-(1+\alpha)O_{j-1/2} - \tfrac{1}{2}\tfrac{\rho_f\sigma_{nf}}{\rho_{nf}\sigma_f}\ M\Big]\\
(m_6)_j &= \ (m_5)_j\\
(m_7)_j &= h_j\left[\frac{\lambda}{2}\left(\frac{\chi\rho_s\ \left(\beta_s/\beta_f\right)\ +(1-\chi)\rho_f}{(1-\chi)\rho_f+\chi\rho_s}\right)\frac{\sin x^{n-1/2}}{x^{n-1/2}}\right]\\
(m_8)_j &= \ (m_7)_j\end{aligned} \tag{40}$$

$$\begin{aligned}\big(n_1\big)_j &= \left[\frac{1}{\mathrm{Pr}}\frac{k_{nf}/k_f}{\Big((1-\chi)(\rho C_p)_f+\chi\big(\rho c_p\big)_s/\big(\rho c_p\big)_f\Big)} + h_j\Big(\tfrac{(1+\alpha)}{2}F_{j-1/2} - \tfrac{\alpha}{2}F^{n-1}_{j-1/2}\Big)\right]\\
(n_2)_j &= \left[\frac{2}{\mathrm{Pr}} \ - \ (b_1)_j\right]\\
(n_3)_j &= h_j\Big[\tfrac{(1+\alpha)}{2}p_{j-1/2} + \tfrac{\alpha}{2}I^{n-1}_{j-1/2}\Big]\\
\big(n_4\big)_j &= (n_3)_j\\
(n_5)_j &= h_j\Big[-\tfrac{\alpha}{2}H_{j-1/2} + \tfrac{\alpha}{2}H^{n-1}_{j-1/2}\Big]h_j\\
(n_6)_j &= (n_5)_j\\
(n_7)_j &= h_j\Big[-\tfrac{\alpha}{2}O_{j-1/2} - \tfrac{\alpha}{2}h_jO^{n-1}_{j-1/2}\Big]\\
(n_8)_j &= (n_7)_j\end{aligned} \tag{41}$$

$$\begin{aligned}(r_1)_{j-1/2} \ &= \ F_{j-1} - F_j + h_jO_{j-1/2}\\
(r_2)_{j-1/2} &= O_{j-1} - O_j + h_jQ_{j-1/2}\\
(r_3)_{j-1/2} &= H_{j-1} - H_j + h_jI_{j-1/2}\\
(r_4)_{j-1/2} \ &= \frac{\rho_f}{\rho_{nf}}\frac{1}{(1-\chi)^{2.5}}\Big(1+\tfrac{1}{\beta}\Big)\ (Q_{j-1} - Q_j) - (1+\alpha)h_j\ F_{j-1/2}Q_{j-1/2}\\
+h_j\ &\left(\alpha Q_{j-1/2}F^{n-1}_{j-1/2} - \alpha Q^{n-1}_{j-1/2}\ F_{j-1/2} - \frac{\sin x^{n-1/2}\cos x^{n-1/2}}{x^{n-1/2}} + \frac{M}{2}\frac{\sin x^{n-1/2}}{x^{n-1/2}}\right)\\
&-h_j\left(\frac{\chi\rho_s\ \left(\beta_s/\beta_f\right)\ +(1-\chi)\rho_f}{(1-\chi)\rho_f+\chi\rho_s}\right)\lambda\frac{\sin x^{n-1/2}}{x^{n-1/2}}g_{j-1/2}\end{aligned} \tag{42}$$

$$\begin{aligned}(r_5)_{j-1/2} = \frac{1}{\mathrm{Pr}}\frac{k_{nf}/k_f}{\Big((1-\chi)(\rho C_p)_f+\chi\big(\rho c_p\big)_s/\big(\rho c_p\big)_f\Big)}\Big(t_{j-1} - t_j\Big) - \alpha h_jt^{n-1}_{j-1/2}F_{j-1/2}\\
-(1+\alpha)h_jF_{j-1/2}t_{j-1/2} + \alpha h_jt_{j-1/2}F^{n-1}_{j-1/2} + \alpha h_jw_{j-1/2}s_{j-1/2}\\
-\alpha h_jw_{j-1/2}s^{n-1}_{j-1/2} + \alpha h_jw^{n-1}_{j-1/2}s_{j-1/2} \ + (R_2)^{n-1}_{j-1/2}\end{aligned}$$

3.3. The Block Tridiagonal Matrix

The matrix form of the linearized tridiagonal system is:

$$\mathrm{W}\delta = \mathrm{r}, \tag{43}$$

where

$$\mathrm{W} = \begin{bmatrix} [M_1] & [L_1] & & & & & \\ [N_2] & [M_2] & [L_2] & & & & \\ & & \ddots & & & & \\ & & & \ddots & & & \\ & & & & \ddots & & \\ & & & & [N_{J-1}] & [M_{J-1}] & [L_{J-1}] \\ & & & & & [N_J] & [L_J] \end{bmatrix}, \quad \delta = \begin{bmatrix} [\delta_1] \\ [\delta_2] \\ \vdots \\ [\delta_{J-1}] \\ [\delta_J] \end{bmatrix}, \mathrm{r} = \begin{bmatrix} [r_1] \\ [r_2] \\ \vdots \\ [r_{J-1}] \\ [r_J] \end{bmatrix}.$$

Boundary conditions (34) are satisfied with no iteration. This is attributed to maintaining appropriate values in each iteration. We suppose that $\delta F_0 = 0$, $\delta O_0 = 0$, $\delta I_0 = 0$, $\delta w_J = 0$, $\delta H_J = 0$, and $d_J = -\frac{1}{2} h_J$.

The entries of the matrices are:

$$[M_1] = \begin{bmatrix} 0 & 0 & 1 & 0 & 0 \\ d_1 & 0 & 0 & d_1 & 0 \\ 0 & -1 & 0 & 0 & d_1 \\ (m_2)_1 & (m_8)_1 & (m_3)_1 & (m_1)_1 & 0 \\ 0 & (n_8)_1 & (n_3)_1 & 0 & (n_1)_1 \end{bmatrix} \tag{44}$$

$$[M_j] = \begin{bmatrix} d_j & 0 & 0 & 0 & 0 \\ -1 & 0 & 0 & 0 & 0 \\ 0 & -1 & 0 & 0 & 0 \\ (m_6)_j & (m_8)_j & (m_3)_j & (m_1)_j & 0 \\ (n_6)_j & (n_8)_j & (n_3)_j & 0 & (n_1)_j \end{bmatrix}, \; 2 \le j \le J, \tag{45}$$

$$[N_j] = \begin{bmatrix} 0 & 0 & -1 & 0 & 0 \\ 0 & 0 & 0 & d_j & 0 \\ 0 & 0 & 0 & 0 & d_j \\ 0 & 0 & (m_4)_j & (m_2)_j & 0 \\ 0 & 0 & (n_4)_j & 0 & (n_2)_j \end{bmatrix}, \; 2 \le j \le J, \tag{46}$$

$$[L_j] = \begin{bmatrix} d_j & 0 & 0 & 0 & 0 \\ 1 & 0 & 0 & 0 & 0 \\ 0 & 1 & 0 & 0 & 0 \\ (m_5)_j & (m_7)_j & 0 & 0 & 0 \\ (n_5)_j & (n_7)_j & 0 & 0 & 0 \end{bmatrix}, \; 1 \le j \le J-1, \tag{47}$$

$$[\delta_1] = \begin{bmatrix} \delta Q_0 \\ \delta H_0 \\ \delta F_1 \\ \delta Q_1 \\ \delta I_1 \end{bmatrix}, [\delta_j] = \begin{bmatrix} \delta O_{j-1} \\ \delta H_{j-1} \\ \delta F_{j-1} \\ \delta Q_{j-1} \\ \delta I_{j-1} \end{bmatrix}, 2 \le j \le J, \; [r_j] = \begin{bmatrix} (r_1)_{j-(1/2)} \\ (r_2)_{j-(1/2)} \\ (r_3)_{j-(1/2)} \\ (r_4)_{j-(1/2)} \\ (r_5)_{j-(1/2)} \end{bmatrix}, 1 \le j \le J \tag{48}$$

Finally, the lower–upper decomposition method is employed to solve the system (43). The MATLAB program has been used to perform numerical calculations considering the wall shear stress δQ_0 as a convergence criterion, which is often employed in laminar boundary layer computations to achieve the required accuracy. This is most likely due to the fact that the wall shear stress in the laminar boundary layer calculations has the maximum error (see Cebeci and Bradshaw [79]). The iterations are implemented until some convergence criterion is obtained, and terminated when $\left|\delta Q_0^{(i)}\right| < \varepsilon_1$. However, $\varepsilon_1 = 10^{-7}$ is selected to be 10^{-7}, which gives precision to our results up to six decimal places.

4. Results and Discussion

In this section, MATLAB was employed to perform the numerical computations to acquire graphical and numerical findings for the flow characteristics of kerosene oil as a host Casson nanoliquid, considering the influence of some relevant parameters, as well as providing a thorough parametric analysis. In such an analysis, the numerical results are observed when a single examinable parameter varies over the range, whereas other examinable parameters remain constant. It is a typical analysis usually used by mathematicians, physicists, and engineers in modeling and decision-making. The parameters that were taken into account in the calculations are mixed convection λ, magnetic M, Casson β, and nanoparticle volume fraction χ and have ranges of. $-1.5 \leq \lambda \leq 10,\ 0.1 \leq \chi \leq 0.2$,$M > 0,$ and $\beta > 0$.

Table 1 states the thermophysical properties of kerosene oil and the ultrafine particles that were employed in this work. In order to emphasize the accuracy of the current work's outcomes, the approximate relative error ε_a is calculated between the current and previous outcomes in Tables 2 and 3 using the following formula:

$$\varepsilon_a = \frac{|R_c - R_p|}{R_c} \times 100\% \tag{49}$$

Table 1. Thermo-physical properties of Kerosene oil and nanoparticles [14,29,41,80].

Thermo-Physical Property	Kerosene Oil	Al_2O_3	TiO_2	ZnO
$\rho\left(\mathrm{kg/m^3}\right)$	783	3970	4230	5600
$C_p(\mathrm{J/kgK})$	2090	765	650	502.7
$K(\mathrm{w/mK})$	0.15	40	8.9528	13
$\beta \times 10^{-5}(\mathrm{K}^{-1})$	21	0.85	0.9	0.431
$\sigma(\mathrm{S/m})$	5×10^{-11}	35×10^{6}	2.6×10^{6}	1×10^{-2}
Pr	22.85	-	-	-

Table 2. Validation of $\mathrm{Re}^{1/2}C_f$ by comparing it with Tham's et al. [66] findings for different values of λ ($\beta \to \infty,\ M = 0,\ \chi = 0,\ \mathrm{Pr} = 1$) .

λ		-0.5			0			2	
x	Tham et al.	Present	ε_a (%)	Tham et al.	Present	ε_a (%)	Tham et al.	Present	ε_a (%)
0	0.0000	0.0000	0.0000	0.0000	0.0000	0.0000	0.0000	0.0000	0.0000
0.2	0.1869	0.1868	0.0500	0.2425	0.2437	0.4900	0.4349	0.4136	0.4800
0.4	0.3503	0.3503	0.0000	0.4619	0.4573	0.9900	0.8452	0.8456	0.0500
0.6	0.4690	0.4689	0.0200	0.6377	0.6347	0.4700	1.2084	1.1996	0.7300
0.8	0.5244	0.5235	0.1700	0.7525	0.7519	0.0700	1.5061	1.4929	0.8700
1.0	0.5012	0.5048	0.7100	0.7944	0.7965	0.2600	1.7252	1.7161	0.5200
1.2	0.3834	0.3825	0.2300	0.7566	0.7615	0.6400	1.8586	1.8539	0.2500
1.4	0.1138	0.1134	0.3500	0.6370	0.6347	0.3600	1.9060	1.9056	0.0200
1.6				0.4333	0.4343	0.2300	1.8735	1.8769	0.1800
1.8				0.0934	0.0888	0.4900	1.7726	1.7791	0.3600
2.0							1.6188	1.6275	0.5300
2.2							1.4297	1.4397	0.6900
2.4							1.2225	1.2331	0.8600
2.6							1.0116	1.0121	0.0500
2.8							0.8052	0.8054	0.0200
3.0							0.6029	0.6031	0.0300
π							0.4564	0.4564	0.0000

Table 3. Validation of $\mathrm{Re}^{-1/2}Nu$ by comparing it with Tham's et al. [66] findings for different values of λ ($\beta \to \infty$, $M = 0$, $\chi = 0$, $\mathrm{Pr} = 1$).

λ		-0.5			0			2	
x	**Tham et al.**	**Present**	ε_a **(%)**	**Tham et al.**	**Present**	ε_a **(%)**	**Tham et al.**	**Present**	ε_a **(%)**
0	0.5421	0.5421	0.0000	0.5705	0.5705	0.0000	0.6515	0.6515	0.0000
0.2	0.5379	0.5383	0.0700	0.5668	0.5672	0.0700	0.6487	0.6490	0.0400
0.4	0.5257	0.5264	0.1300	0.5563	0.5569	0.1000	0.6407	0.6411	0.0600
0.6	0.5050	0.5049	0.0100	0.5387	0.5395	0.1400	0.6275	0.6273	0.0300
0.8	0.4751	0.4752	0.0200	0.5140	0.5139	0.0100	0.6094	0.6101	0.1100
1.0	0.4342	0.4343	0.0200	0.4818	0.4837	0.3900	0.5867	0.5864	0.0500
1.2	0.3766	0.3770	0.1000	0.4415	0.4417	0.0400	0.5598	0.5596	0.0300
1.4	0.2683	0.2692	0.3300	0.3914	0.3917	0.0700	0.5292	0.5291	0.0100
1.6				0.3260	0.3266	0.1800	0.4955	0.4972	0.3400
1.8				0.2051	0.2068	0.8200	0.4595	0.4594	0.0200
2.0							0.4219	0.4219	0.0000
2.2							0.3837	0.3856	0.4900
2.4							0.3458	0.3458	0.0000
2.6							0.3090	0.3108	0.5800
2.8							0.2737	0.2737	0.0000
3.0							0.2394	0.2411	0.7100
π							0.2144	0.2144	0.0000

Here, R_c and R_p are the current and previous results, respectively.

It was found that the errors are sufficiently small, making our numerical outcomes compatible with previous results.

At the outset, it is appropriate to mention here the occurrence of separation point phenomena in the laminar boundary layer, which is one of the most important aspects of the movement of an incompressible fluid around a solid body. This phenomenon appears clearly in Tables 2 and 3, as it appears in Figures 2 and 3. It has been addressed by many researchers [81–84].

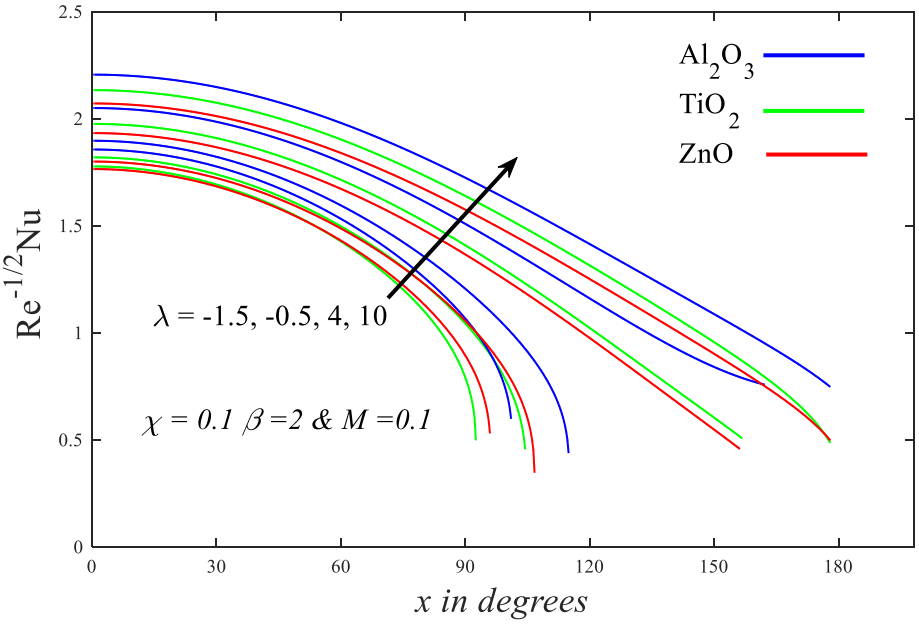


Figure 2. Impression of λ on $\mathrm{Re}^{-1/2}Nu$.

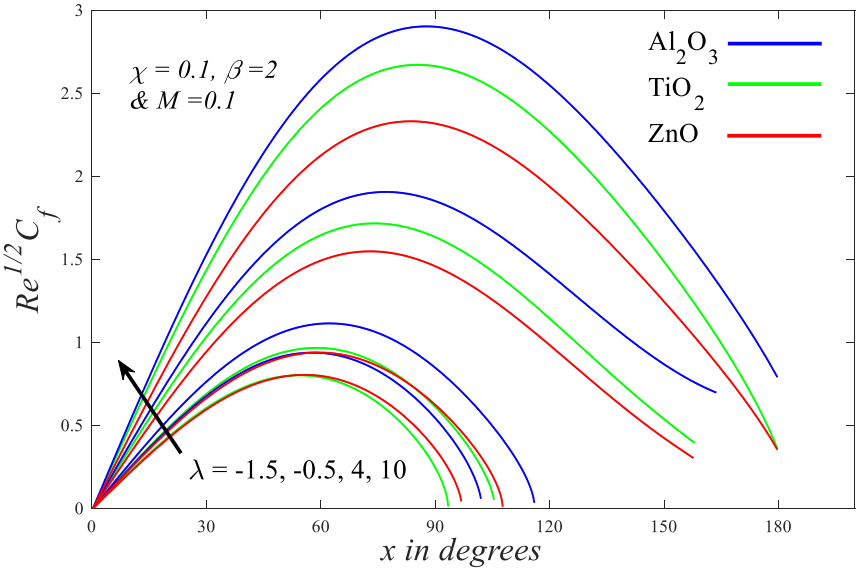


Figure 3. Impression of λ on $\mathrm{Re}^{1/2}C_f$.

Figures 2 and 3 depict the impression of the combined convection parameter on the Nusselt number and skin friction in both flow states ($\lambda < 0$ & $\lambda > 0$) with volume fraction fixed at $\chi = 0.1$, Casson parameter at $\beta = 2$, and magnetic parameter $M = 0.1$. It can be observed from Figure 2 that an ascending trend of the mixed convection parameter is accompanied by a rising Nusselt number. This occurs due to the enhancement of the buoyancy forces, which are produced by the increasing combined convection parameter. According to Figure 3, as the values of the combined convection parameter grow, the skin friction follows the same tendency as the Nusselt number. This is due to an increase in buoyancy forces too.

Figures 4 and 5 are related to the influence of ultrafine particle volume fraction on Nusselt number and skin friction, while keeping the rest of the parameters constant ($\lambda = 10,\ \beta = 2\ $ & $M = 0.1$). One can see that in Figures 4 and 5, with elevating values of nanoparticle volume fraction, both Nusselt number and skin friction improve. This is expected because the growth in nanoparticle volume fraction leads to an enhancement in thermal conductivity for kerosene oil and, consequently, an augmentation in Nusselt number and skin friction.

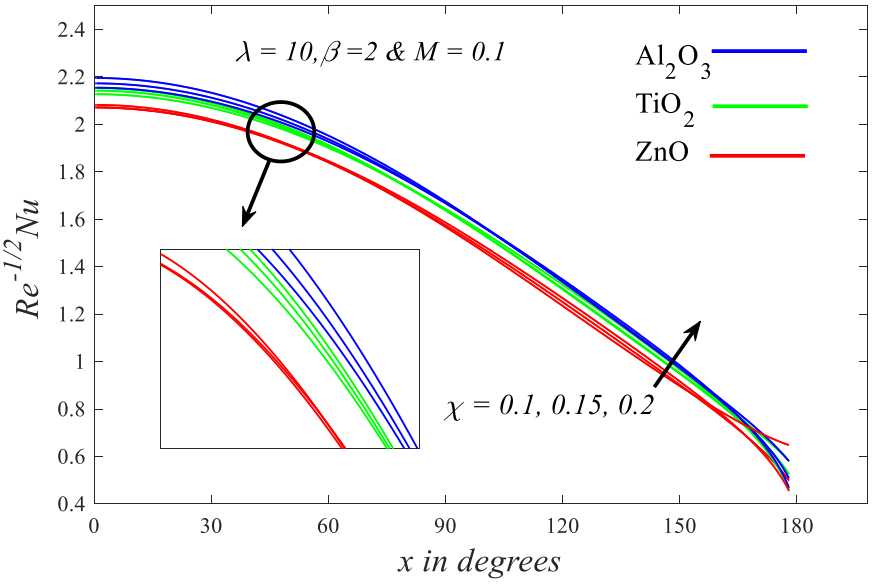


Figure 4. Impression of χ on $\mathrm{Re}^{-1/2}Nu$. The inset is a partial enlargement of the curves.

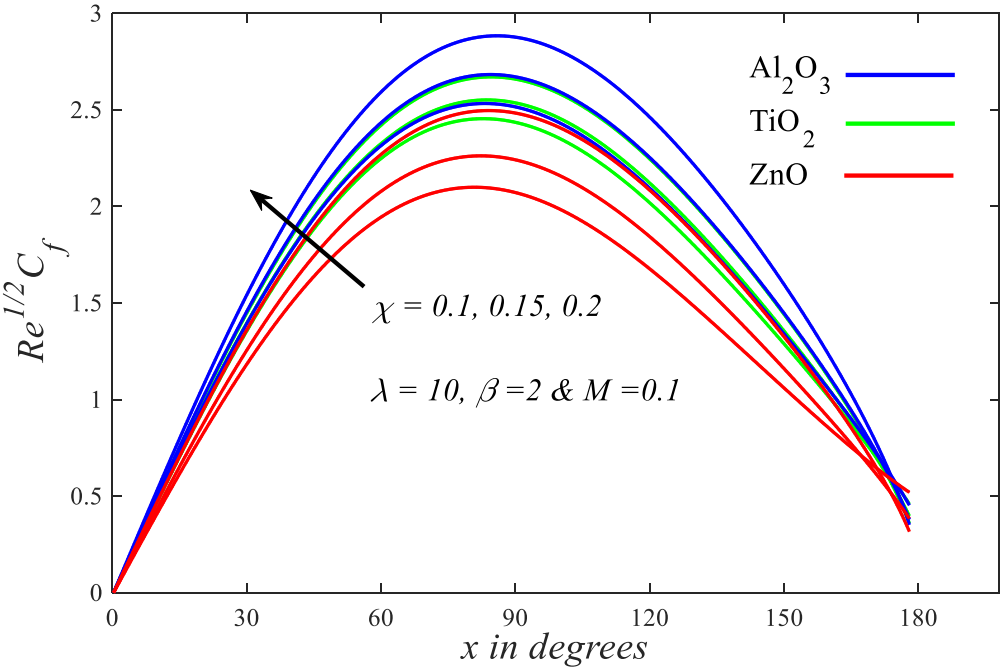


Figure 5. Impression of χ on $\mathrm{Re}^{1/2}C_f$.

The variation of Nusselt number and skin friction with the Casson parameter are shown in Figures 6 and 7, respectively. It can be seen that the Casson parameter has a positive effect on Nusselt number while it has a negative effect on skin friction. Physically, increasing the Casson parameter leads to a decrease in yield stress, which in turn reduces skin friction. At the same time, the higher values of the Casson parameter reduce the viscosity of the fluid, which contributes to an increase in heat transmission and, thus, an increase in the Nusselt number.

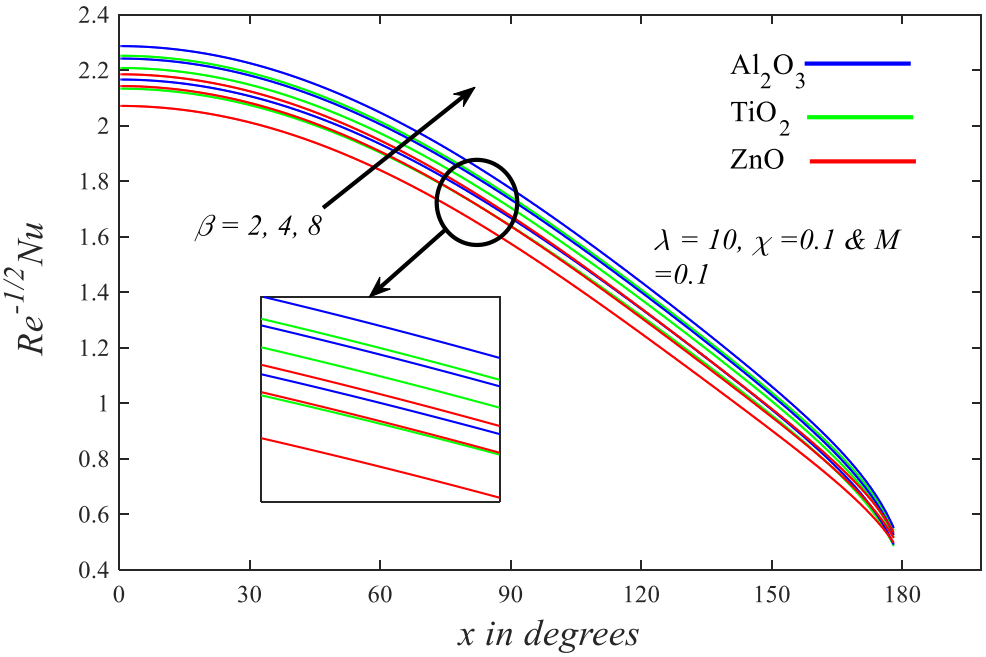


Figure 6. Impression of β on $\mathrm{Re}^{-1/2}Nu$. The inset is a partial enlargement of the curves.

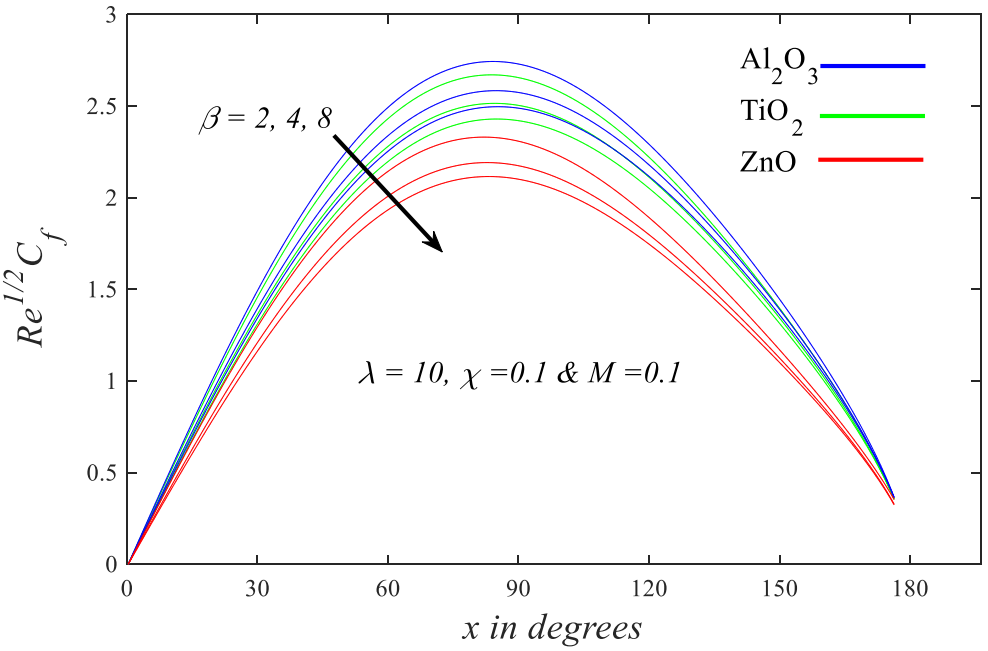


Figure 7. Impression of β on $\mathrm{Re}^{1/2}C_f$.

Figures 8 and 9 show the behavior of the Nusselt number and skin friction when they are affected by an increasing magnetic field. Obviously, the Nusselt number and skin friction are decreasing functions of the magnetic parameter. Actually, this reduction is caused by the curbing of fluid movement caused by an increase in the intensity of the magnetic field, which restrains convection and, thus, both are reduced. Furthermore, the figures above confirm that Al_2O_3–kerosene oil is superior in terms of $\mathrm{Re}^{1/2}C_f$ and $\mathrm{Re}^{-1/2}Nu$, regardless of the value of the parameters λ, χ, β or M.

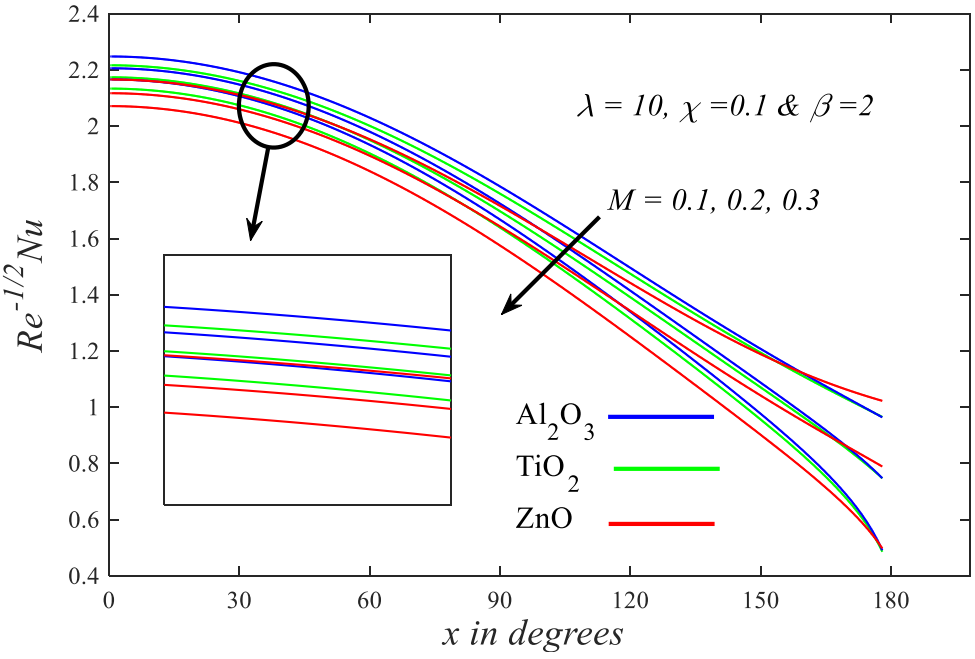


Figure 8. Impression of M on $\mathrm{Re}^{-1/2}Nu$. The inset is a partial enlargement of the curves.

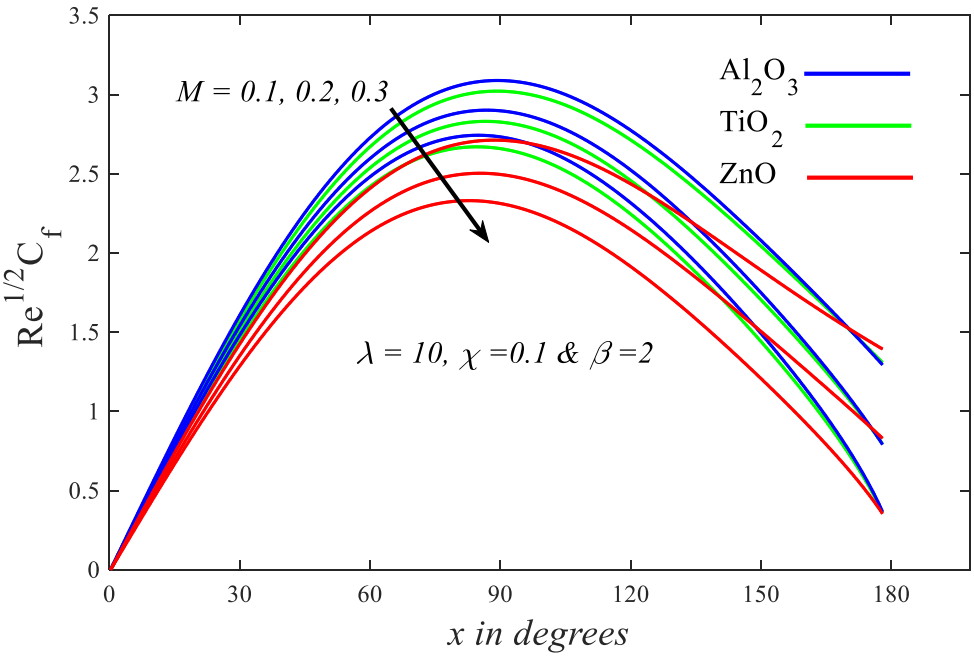


Figure 9. Impression of M on $\mathrm{Re}^{1/2}C_f$.

Figures 10 and 11 illustrate the effect of the combined convection parameter on temperature and velocity, respectively. It is noticed here that by improving the mixed convection parameter, the temperature declines while the velocity grows. This growth in velocity or decline in temperature is due to an increase in the buoyancy force caused by an increase in the mixed convection parameter.

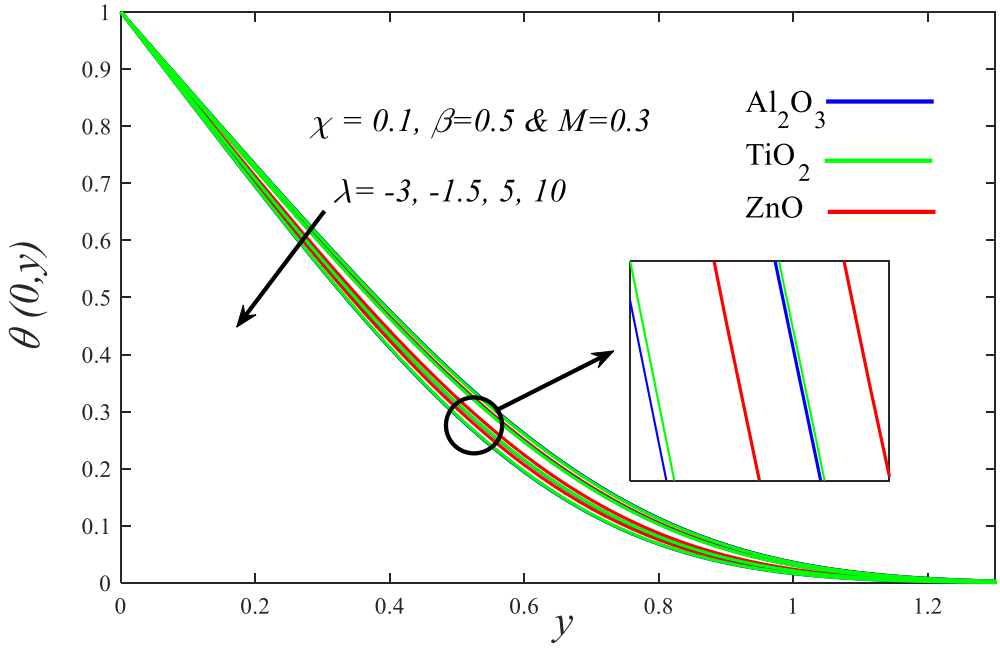


Figure 10. Impression of λ on θ. The inset is a partial enlargement of the curves.

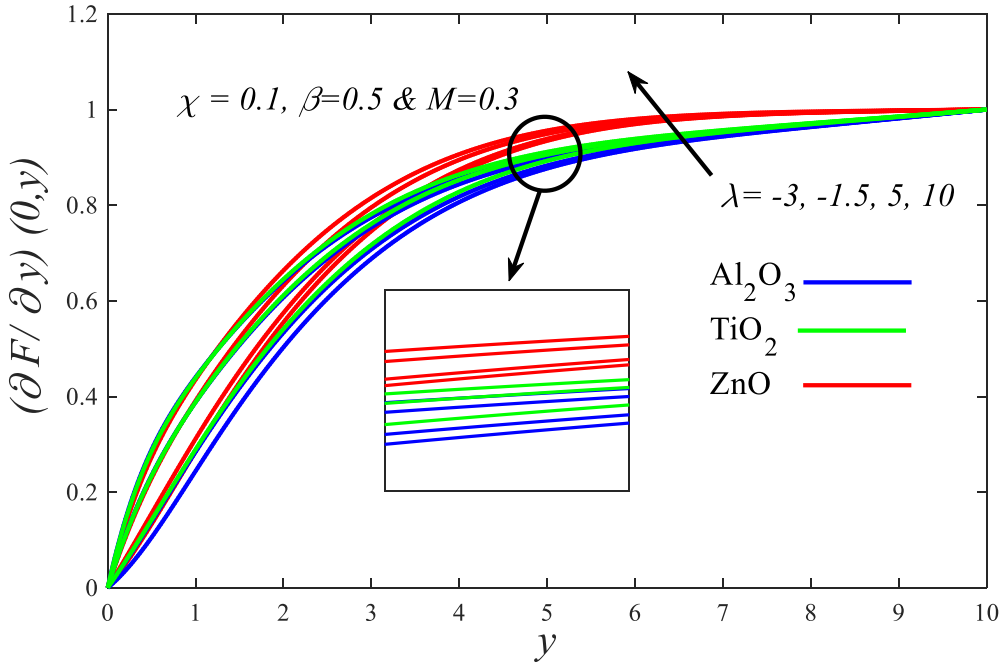


Figure 11. Impression of λ on $\partial F/\partial y$. The inset is a partial enlargement of the curves.

According to Figures 12 and 13, a growing nanoparticle volume fraction causes a heightening in the transmission of heat from outside of the cylinder's surface to the fluid, which aids in raising the thickness of the thermal layer as a result of the augmentation in the temperature of the fluid. Besides, the rise in volume fraction of the nanoparticle for any of the employed reinforcer nanoparticles enhances the thermal conductivity of the host fluid, which results in the rate of heat transfer for the host fluid improving, consequently contributing to its increasing velocity, as is obviously seen in Figure 13.

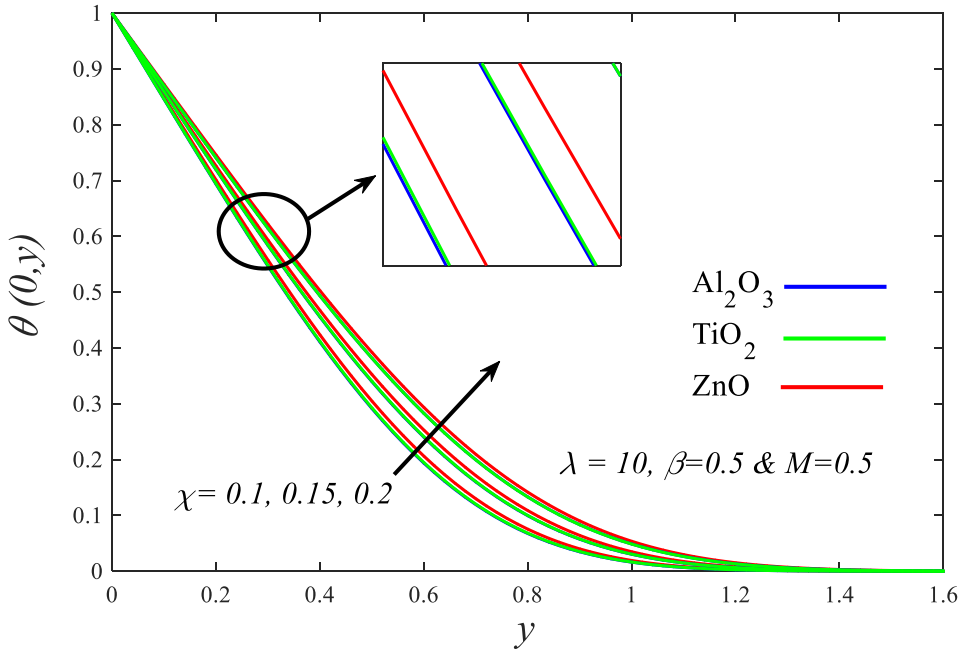


Figure 12. Impression of χ on θ. The inset is a partial enlargement of the curves.

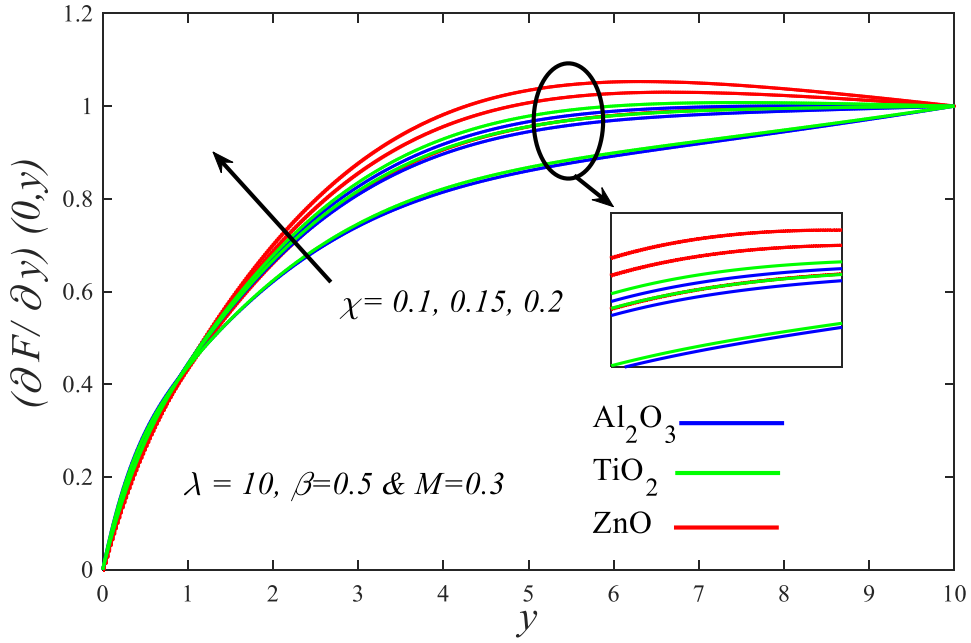


Figure 13. Impression of χ on $\partial F/\partial y$. The inset is a partial enlargement of the curves.

Figures 14 and 15 depict the graphical findings of temperature and velocity versus the Casson parameter. The increase in the Casson parameter will inhibit temperature and velocity. The augmentation in the Casson parameter causes a decrease in the fluid viscosity, thereby the temperature decay. On the other hand, the increase in Casson factor values is followed by a decrease in the yield stress of the Casson fluid, as well as an increase in the plastic dynamic viscosity. This rise produces resistance in the fluid flow, which acts to limit the fluid velocity. See Figure 15 for details.

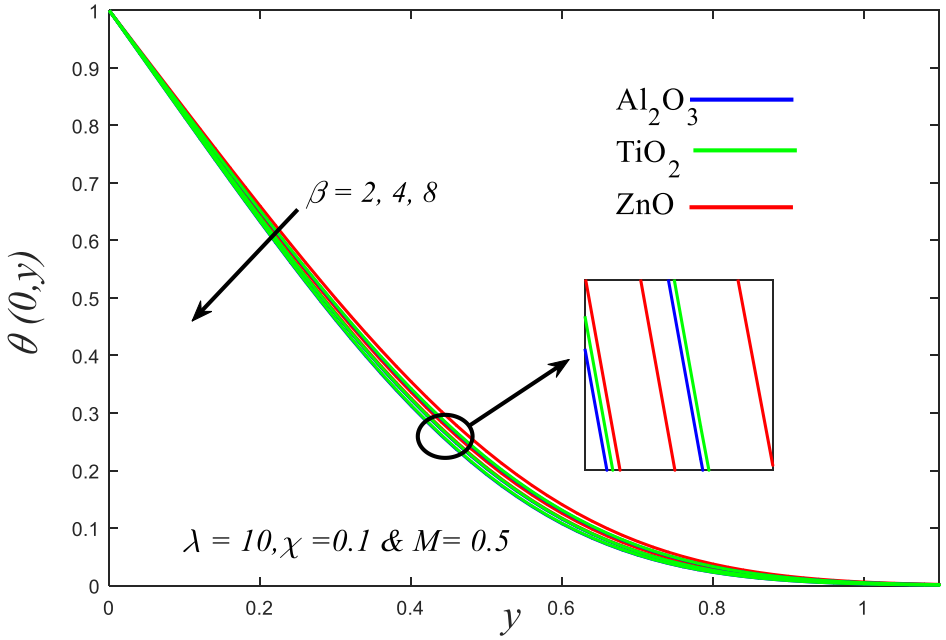


Figure 14. Impression of β on θ. The inset is a partial enlargement of the curves.

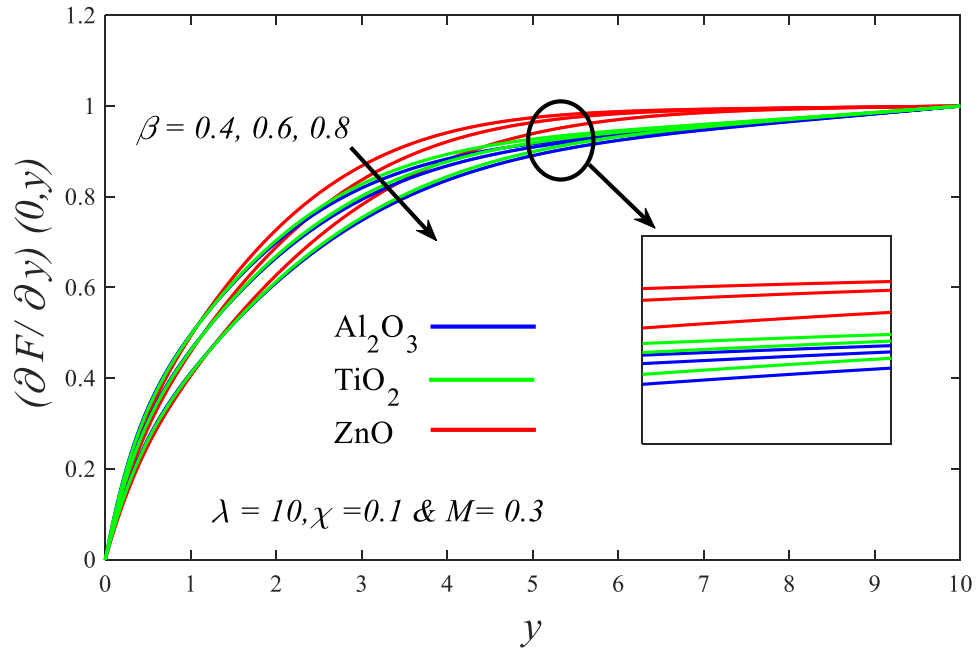


Figure 15. Impression of β on $\partial F/\partial y$. The inset is a partial enlargement of the curves.

Figures 16 and 17 show that with the increasing values of the magnetic parameter, the temperature rises but the velocity reduces. Of course, this will happen because crossing a magnetic field through a moving fluid generates a force called the Lorentz force. This force generates a kind of friction in the flow, which in turn generates more heat energy, which eventually increases the temperature. Additionally, increasing the intensity of the magnetic field aims to strengthen the force of friction, which curbs the flow of the fluid and slows its velocity. It is also noticed that zinc oxide–kerosene oil gains the highest velocity and temperature regardless of the values of the parameters affecting it.

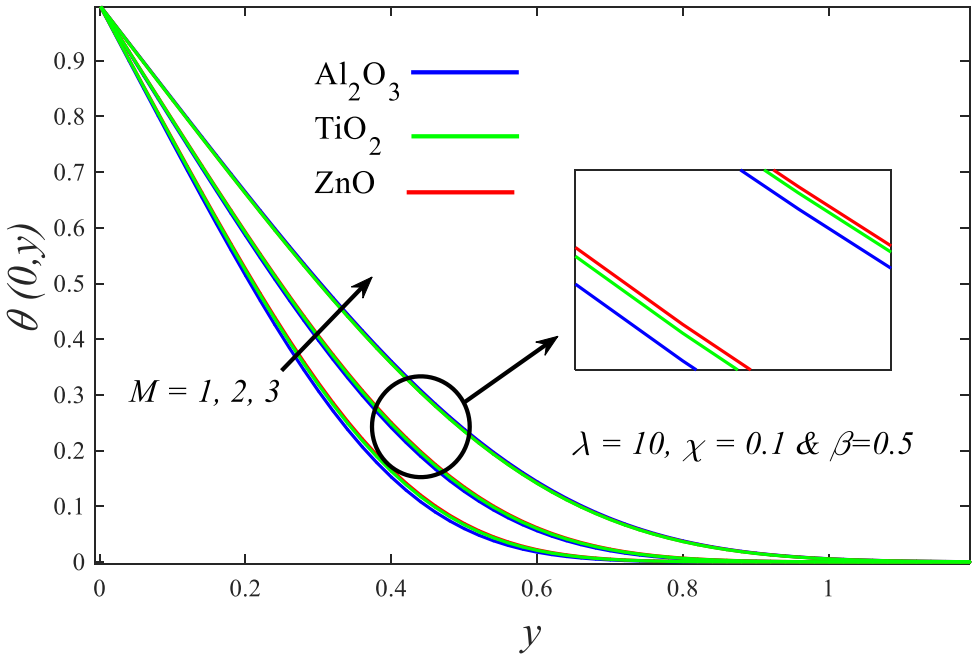


Figure 16. Impression of M on θ. The inset is a partial enlargement of the curves.

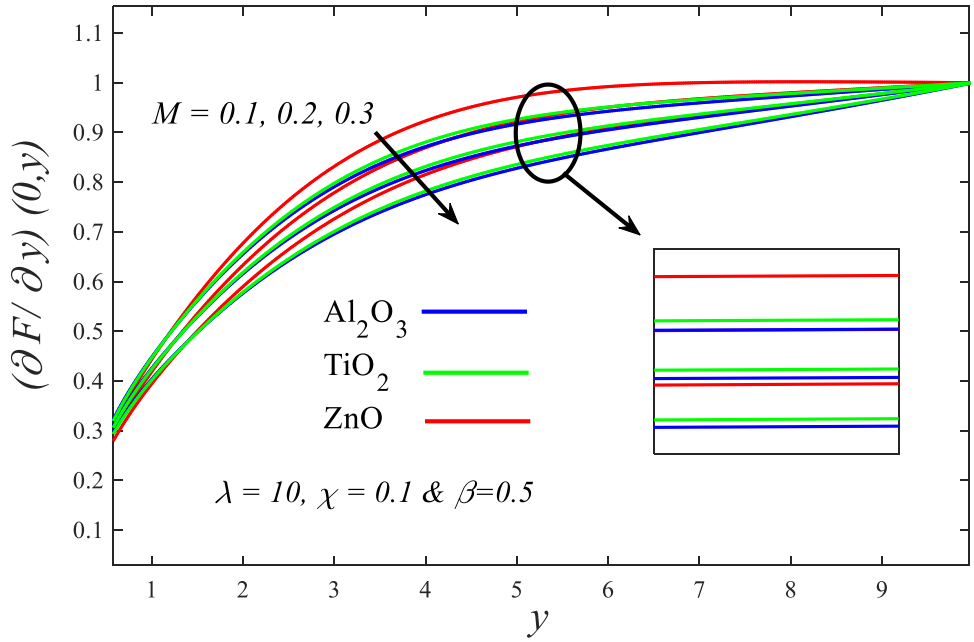


Figure 17. Impression of M on $\partial F/\partial y$. The inset is a partial enlargement of the curves.

5. Conclusions

In this work, the impact of combined convection, magnetic parameter, Casson parameter, and the volume fraction of nanoparticles on physical quantities that are heat transfer-related were numerically examined to achieve a comprehensive view of the energy transmission characteristics of kerosene oil-based Casson nanoliquid flowing around a circular cylinder, taking into account the combined convection and magnetic forces. Graphical results were obtained, discussed, and analyzed. The following meaningful remarks deserve mention:

1. All the physical quantities studied in this work showed increasing behavior when the values of ultrafine particle volume fraction grew.
2. Temperature possesses an inverse relationship with β or λ, while it has a direct relationship with M.
3. Velocity is a decreasing function of M or β, while it is an increasing function of λ.
4. Increasing λ increases $\mathrm{Re}^{1/2}C_f$, but increasing M or β decreases it.
5. The growth of each of the values of β or λ boosts the rate of energy transport, whereas the growth of the values of M decays it.
6. Whatever the values of the parameters examined in this article, Al_2O_3–kerosene oil has the highest heat transmission rate and skin friction. Moreover, it has the lowest temperature.

Author Contributions: Conceptualization, R.I.; methodology, H.T.A. and F.A.A.; software, H.T.A. and F.A.A.; validation, A.S.H.; formal analysis, H.T.A. and A.S.H.; investigation, F.A.A.; resources, R.I., H.T.A. and A.S.H.; writing—original draft preparation, F.A.A.; supervision, R.I. All authors have read and agreed to the published version of the manuscript.

Funding: The authors extend their appreciation to the Deputyship for Research & Innovation, Ministry of Education in Saudi Arabia for funding this research work through the project number (IF-PSAU-2021/01/18027).

Institutional Review Board Statement: Not applicable.

Informed Consent Statement: Not applicable.

Data Availability Statement: Data sharing is not available. In this investigation, no new data were generated or examined. This article does not deal with data sharing.

Conflicts of Interest: The authors state that they have no conflict of interest.

Nomenclature

a	Radius of Cylinder (m)	T	Temperature of the fluid (K)
B_0	Magnetic field strength (kg /s^2 A)	T_w	Wall temperature (K)
C_f .	Skin friction coefficient	T_∞	Ambient temperature (K)
Gr	Grashof number	u	ξ-component of velocity (m/s)
g	Gravity vector	v	η-component of velocity (m/s)
k	Thermal conductivity (W/mK)	v_f	Kinematic viscosity (m^2 /s)
M	Magnetic parameter	u_e	Velocity of external flow (m/s)
Nu	Nusselt Number		Free stream velocity (m/s)
Pr	Prandtl number		
p_y	Yield stress (N/m^2)		
Re	Reynolds number		
Subscribt			
s	Nanoparticles	nf	Nanoliquid
f	base fluid		

References

1. Dash, R.; Mehta, K.; Jayaraman, G. Casson fluid flow in a pipe filled with a homogeneous porous medium. *Int. J. Eng. Sci.* **1996**, *34*, 1145–1156. [CrossRef]
2. Casson, N. A flow equation for pigment-oil suspensions of the printing ink type. *Rheol. Disperse Syst.* **1959**, *2*, 84–102.
3. Askadsky, A. *Rheology of Polymers*; Vinogradov, G.V., Malkin, A.Y., Eds.; Khimiya Publishers: Moscow, Russia, 1977; p. 438. (In Russian)
4. Walawender, W.P.; Chen, T.Y.; Cala, D.F. An approximate Casson fluid model for tube flow of blood. *Biorheology* **1975**, *12*, 111–119. [CrossRef]
5. Blair, G.S. An equation for the flow of blood, plasma and serum through glass capillaries. *Nature* **1959**, *183*, 613–614. [CrossRef] [PubMed]
6. Ali, A.; Bukhari, Z.; Umar, M.; Ismail, M.A.; Abbas, Z. Cu and Cu-SWCNT Nanoparticles' Suspension in Pulsatile Casson Fluid Flow via Darcy–Forchheimer Porous Channel with Compliant Walls: A Prospective Model for Blood Flow in Stenosed Arteries. *Int. J. Mol. Sci.* **2021**, *22*, 6494. [CrossRef]
7. Mustafa, M.; Hayat, T.; Pop, I.; Aziz, A.l. Unsteady boundary layer flow of a Casson fluid due to an impulsively started moving flat plate. *Heat Tran. Asian Res.* **2011**, *40*, 563–576. [CrossRef]
8. Mukhopadhyay, S.; De, P.R.; Bhattacharyya, K.; Layek, G. Casson fluid flow over an unsteady stretching surface. *Ain Shams Eng. J.* **2013**, *4*, 933–938. [CrossRef]
9. Khalid, A.; Khan, I.; Khan, A.; Shafie, S. Unsteady MHD free convection flow of Casson fluid past over an oscillating vertical plate embedded in a porous medium. *Eng. Sci. Technol. Int. J.* **2015**, *18*, 309–317. [CrossRef]
10. Animasaun, I.; Adebile, E.; Fagbade, A. Casson fluid flow with variable thermo-physical property along exponentially stretching sheet with suction and exponentially decaying internal heat generation using the homotopy analysis method. *J. Niger. Math. Soc.* **2016**, *35*, 1–17. [CrossRef]
11. EL-Kabeir, S.; El-Zahar, E.; Rashad, A. Effect of chemical reaction on heat and mass transfer by mixed convection flow of casson fluid about a sphere with partial slip. *J. Comput. Theor. Nanosci.* **2016**, *13*, 5218–5226. [CrossRef]
12. Makinde, O.; Sandeep, N.; Ajayi, T.; Animasaun, I. Numerical exploration of heat transfer and Lorentz force effects on the flow of MHD Casson fluid over an upper horizontal surface of a thermally stratified melting surface of a paraboloid of revolution. *Int. J. Nonlinear Sci. Numer. Simul.* **2018**, *19*, 93–106. [CrossRef]
13. Thumma, T.; Wakif, A.; Animasaun, I.L. Generalized differential quadrature analysis of unsteady three-dimensional MHD radiating dissipative Casson fluid conveying tiny particles. *Heat Transf.* **2020**, *49*, 2595–2626. [CrossRef]
14. Alwawi, F.A.; Alkasasbeh, H.T.; Rashad, A.; Idris, R. MHD natural convection of Sodium Alginate Casson nanofluid over a solid sphere. *Res. Phys.* **2020**, *16*, 102818. [CrossRef]
15. Alwawi, F.A.; Alkasasbeh, H.T.; Rashad, A.; Idris, R. Heat transfer analysis of ethylene glycol-based Casson nanofluid around a horizontal circular cylinder with MHD effect. *Proc. Inst. Mech. Eng. C. J. Mech. Eng. Sci.* **2020**, *234*, 2569–2580. [CrossRef]
16. Gul, T.; Ali, B.; Alghamdi, W.; Nasir, S.; Saeed, A.; Kumam, P.; Mukhtar, S.; Kumam, W.; Jawad, M. Mixed convection stagnation point flow of the blood based hybrid nanofluid around a rotating sphere. *Sci. Rep.* **2021**, *11*, 7460. [CrossRef]
17. Alwawi, F.A.; Alkasasbeh, H.T.; Rashad, A.M.; Idris, R. Natural convection flow of Sodium Alginate based Casson nanofluid about a solid sphere in the presence of a magnetic field with constant surface heat flux. *J. Phys. Conf. Ser.* **2019**, *1366*, 012005. [CrossRef]
18. Choi, S.U.; Eastman, J.A. *Enhancing Thermal Conductivity of Fluids with Nanoparticles*; Argonne National Lab.: Aurora, IL, USA, 1995.

19. Eastman, J.A.; Choi, S.; Li, S.; Yu, W.; Thompson, L. Anomalously increased effective thermal conductivities of ethylene glycol-based nanofluids containing copper nanoparticles. *Appl. Phys. Lett.* **2001**, *78*, 718–720. [CrossRef]
20. Suganthi, K.; Vinodhan, V.L.; Rajan, K. Heat transfer performance and transport properties of ZnO–ethylene glycol and ZnO–ethylene glycol–water nanofluid coolants. *Appl. Energy* **2014**, *135*, 548–559. [CrossRef]
21. Han, D.; He, W.; Asif, F. Experimental study of heat transfer enhancement using nanofluid in double tube heat exchanger. *Energy Procedia* **2017**, *142*, 2547–2553. [CrossRef]
22. Dareh, F.R.; Haghshenasfard, M.; Esfahany, M.N.; Jazi, H.R.S. An experimental investigation of pool boiling characteristics of alumina-water nanofluid over micro-/nanostructured surfaces. *Heat Transf. Eng.* **2019**, *40*, 1691–1708. [CrossRef]
23. Hu, B.; Zhang, S.; Wang, D.; Chen, X.; Si, X.; Zhang, D. Experimental study of nucleate pool boiling heat transfer of self-rewetting solution by surface functionalization with TiO_2 nanostructure. *Can. J. Chem. Eng.* **2019**, *97*, 1399–1406. [CrossRef]
24. Ali, H.M.; Generous, M.M.; Ahmad, F.; Irfan, M. Experimental investigation of nucleate pool boiling heat transfer enhancement of TiO2-water based nanofluids. *Appl. Therm. Eng.* **2017**, *113*, 1146–1151. [CrossRef]
25. Dehghani-Ashkezari, E.; Salimpour, M.R. Effect of groove geometry on pool boiling heat transfer of water-titanium oxide nanofluid. *Heat Mass Transf.* **2018**, *54*, 3473–3481. [CrossRef]
26. Al-Hossainy, A.F.; Eid, M.R. Structure, DFT calculations and heat transfer enhancement in [ZnO/PG+ H_2O] C hybrid nanofluid flow as a potential solar cell coolant application in a double-tube. *J. Mater. Sci. Mater. Electron.* **2020**, *31*, 15243–15257. [CrossRef]
27. Sheikholeslami, M.; Hayat, T.; Alsaedi, A. MHD free convection of Al2O3–water nanofluid considering thermal radiation: A numerical study. *Int. J. Heat Mass Transf.* **2016**, *96*, 513–524. [CrossRef]
28. Sawicka, D.; Baars, A.; Cieśliński, J.T.; Smoleń, S. Numerical simulation of natural convection of Glycol-Al2O3 nanofluids from a horizontal cylinder. *Heat Transf. Eng.* **2021**, *42*, 328–336. [CrossRef]
29. Minea, A.A.; Lorenzini, G. A numerical study on ZnO based nanofluids behavior on natural convection. *Int. J. Heat Mass Transf.* **2017**, *114*, 286–296. [CrossRef]
30. Demir, H.; Dalkilic, A.; Kürekci, N.; Duangthongsuk, W.; Wongwises, S. Numerical investigation on the single phase forced convection heat transfer characteristics of TiO2 nanofluids in a double-tube counter flow heat exchanger. *Int. Commun. Heat Mass Transf.* **2011**, *38*, 218–228. [CrossRef]
31. Burggraf, J.; Farber, P.; Karpaiya, K.R.; Ueberholz, P. Numerical Investigation of Laminar Flow Heat Transfer of TiO2-Water Nanofluid in a Heated Pipe. *Heat Transf. Eng.* **2020**, *42*, 1635–1647. [CrossRef]
32. Terenzi, A.; Marchetti, B.; Leporini, M.; Poesio, P.; Liu, J. *Experimental and Numerical Study of Multiphase Flow Phenomena and Models in Oil & Gas Industry*; Elsevier: Amsterdam, The Netherlands, 2019; Volume 5, p. 113.
33. Leporini, M.; Corvaro, F.; Marchetti, B.; Polonara, F.; Benucci, M. Experimental and numerical investigation of natural convection in tilted square cavity filled with air. *Exp. Therm. Fluid Sci.* **2018**, *99*, 572–583. [CrossRef]
34. Giacchetta, G.; Leporini, M.; Marchetti, B.; Terenzi, A. Numerical study of choked two-phase flow of hydrocarbons fluids through orifices. *J. Loss Prev. Process Ind.* **2014**, *27*, 13–20. [CrossRef]
35. Ali, F.; Aamina, K.I.; Sheikh, N.; Gohar, M.; Tlili, I. Effects of different shaped nanoparticles on the performance of engine-oil and kerosene-oil: A generalized Brinkman-type fluid model with non-singular kernel. *Sci. Rep.* **2018**, *8*, 15285. [CrossRef] [PubMed]
36. Hussanan, A.; Salleh, M.Z.; Khan, I.; Shafie, S. Convection heat transfer in micropolar nanofluids with oxide nanoparticles in water, kerosene and engine oil. *J. Mol. Liq.* **2017**, *229*, 482–488. [CrossRef]
37. Ellahi, R.; Zeeshan, A.; Shehzad, N.; Alamri, S.Z. Structural impact of Kerosene-Al2O3 nanoliquid on MHD Poiseuille flow with variable thermal conductivity: Application of cooling process. *J. Mol. Liq.* **2018**, *264*, 607–615. [CrossRef]
38. Afridi, M.; Qasim, M.; Khan, N.A.; Hamdani, M. Heat transfer analysis of Cu–Al2O3–water and Cu–Al2O3–kerosene oil hybrid nanofluids in the presence of frictional heating: Using 3-stage Lobatto IIIA formula. *J. Nanofluids* **2019**, *8*, 885–891. [CrossRef]
39. Swalmeh, M.Z.; Alkasasbeh, H.T.; Hussanan, A.; Mamat, M. Numerical investigation of heat transfer enhancement with Ag-GO water and kerosene oil based micropolar nanofluid over a solid sphere. *J. Adv. Res. Fluid Mech. Therm. Sci.* **2019**, *59*, 269–282.
40. Alkasasbeh, H.T.; Swalmeh, M.Z.; Hussanan, A.; Mamat, M. Numerical Solution of Heat Transfer Flow in Micropolar Nanofluids with Oxide Nanoparticles in Water and Kerosene Oil about a Horizontal Circular Cylinder. *Int. J. Appl. Math.* **2019**, *49*, 1–8.
41. Upreti, H.; Pandey, A.K.; Kumar, M. Thermophoresis and suction/injection roles on free convective MHD flow of Ag–kerosene oil nanofluid. *J. Comput. Des. Eng.* **2020**, *7*, 386–396. [CrossRef]
42. Eid, M.R.; Mabood, F. Entropy analysis of a hydromagnetic micropolar dusty carbon NTs-kerosene nanofluid with heat generation: Darcy–Forchheimer scheme. *J. Therm. Anal. Calorim.* **2021**, *143*, 2419–2436. [CrossRef]
43. Qasim, M.; Khan, Z.H.; Khan, W.A.; Ali Shah, I. MHD boundary layer slip flow and heat transfer of ferrofluid along a stretching cylinder with prescribed heat flux. *PLoS ONE* **2014**, *9*, e83930. [CrossRef] [PubMed]
44. Tamoor, M.; Waqas, M.; Khan, M.I.; Alsaedi, A.; Hayat, T. Magnetohydrodynamic flow of Casson fluid over a stretching cylinder. *Res. Phys.* **2017**, *7*, 498–502. [CrossRef]
45. Alizadeh, R.; Karimi, N.; Nourbakhsh, A. Effects of radiation and magnetic field on mixed convection stagnation-point flow over a cylinder in a porous medium under local thermal non-equilibrium. *J. Therm. Anal. Calorim.* **2020**, *140*, 1371–1391. [CrossRef]
46. Krishna, M.V.; Ahamad, N.A.; Chamkha, A.J. Hall and ion slip impacts on unsteady MHD convective rotating flow of heat generating/absorbing second grade fluid. *Alex. Eng. J.* **2021**, *60*, 845–858. [CrossRef]
47. Rashad, A.; Nabwey, H.A. Gyrotactic mixed bioconvection flow of a nanofluid past a circular cylinder with convective boundary condition. *J. Taiwan Inst. Chem. Eng.* **2019**, *99*, 9–17. [CrossRef]

48. Vijaybabu, T. Influence of porous circular cylinder on MHD double-diffusive natural convection and entropy generation. *Int. J. Mech. Sci.* **2021**, *206*, 106625. [CrossRef]
49. Krishna, M.V.; Chamkha, A.J. Hall and ion slip effects on MHD rotating flow of elastico-viscous fluid through porous medium. *Int. Commun. Heat Mass Transf.* **2020**, *113*, 104494. [CrossRef]
50. Krishna, M.V.; Ahamad, N.A.; Chamkha, A.J. Hall and ion slip effects on unsteady MHD free convective rotating flow through a saturated porous medium over an exponential accelerated plate. *Alex. Eng. J.* **2020**, *59*, 565–577. [CrossRef]
51. Krishna, M.V.; Chamkha, A.J. Hall and ion slip effects on MHD rotating boundary layer flow of nanofluid past an infinite vertical plate embedded in a porous medium. *Res. Phys.* **2019**, *15*, 102652. [CrossRef]
52. Krishna, M.V.; Jyothi, K.; Chamkha, A.J. Heat and mass transfer on MHD flow of second-grade fluid through porous medium over a semi-infinite vertical stretching sheet. *J. Porous Media* **2020**, *23*, 751–765. [CrossRef]
53. Krishna, M.V.; Swarnalathamma, B.; Chamkha, A.J. Investigations of Soret, Joule and Hall effects on MHD rotating mixed convective flow past an infinite vertical porous plate. *J. Ocean. Eng. Sci.* **2019**, *4*, 263–275. [CrossRef]
54. Krishna, M.V.; Reddy, M.G.; Chamkha, A.J. Heat and Mass Transfer on MHD Free Convective Flow over an Infinite Nonconducting Vertical Flat Porous Plate. *Int. J. Fluid Mech. Res.* **2019**, *46*, 1–25. [CrossRef]
55. Krishna, M.V.; Anand, P.; Chamkha, A.J. Heat and mass transfer on free convective flow of amicropolar fluid through a porous surface with inclined magnetic field and hall effects. *Spec. Top. Rev. Porous Media Int. J.* **2019**, *10*, 203–223. [CrossRef]
56. Buongiorno, J. Convective transport in nanofluids. *J. Heat Transfer.* **2006**, *128*, 240–250. [CrossRef]
57. Tiwari, R.K.; Das, M.K. Heat transfer augmentation in a two-sided lid-driven differentially heated square cavity utilizing nanofluids. *Int. J. Heat Mass Transf.* **2007**, *50*, 2002–2018. [CrossRef]
58. Mohamad, A. Heat transfer enhancements in heat exchangers fitted with porous media Part I: Constant wall temperature. *Int. J. Therm. Sci.* **2003**, *42*, 385–395. [CrossRef]
59. Da Riva, E.; Del Col, D. Numerical simulation of laminar liquid film condensation in a horizontal circular minichannel. *J. Heat Transf.* **2012**, *134*, 051019. [CrossRef]
60. Lee, H.C.; Do Oh, B.; Bae, S.W.; Kim, M.H. Single bubble growth in saturated pool boiling on a constant wall temperature surface. *Int. J. Multiph. Flow* **2003**, *29*, 1857–1874. [CrossRef]
61. Lee, H.C.; Oh, B.D.; Bae, S.W.; Kim, M.H.; Lee, J.Y.; Song, I.S. Partial nucleate boiling on the microscale heater maintaining constant wall temperature. *J. Nucl. Sci. Technol.* **2003**, *40*, 768–774. [CrossRef]
62. Merkin, J. Free convection boundary layer on an isothermal horizontal cylinder. In *Heat Transfer Conference, St. Louis, MO, USA, 9–11 August 1976*; American Society of Mechanical Engineers and American Institute of Chemical Engineers: St. Louis, MO, USA, 1976; p. 5.
63. Merkin, J. Mixed convection from a horizontal circular cylinder. *Int. J. Heat Mass Transf.* **1977**, *20*, 73–77. [CrossRef]
64. Nazar, R.; Amin, N.; Pop, I. Mixed convection boundary-layer flow from a horizontal circular cylinder in micropolar fluids: Case of constant wall temperature. *Int. J. Numer. Method H.* **2003**, *13*, 86–109. [CrossRef]
65. Nazar, R.; Amin, N.S.; Pop, I. Mixed convection boundary layer flow from a horizontal circular cylinder in a micropolar fluid: Case of constant wall heat flux. *Int. J. Fluid Mech. Res.* **2004**, *31*, 143–159. [CrossRef]
66. Tham, L.; Nazar, R.; Pop, I. Mixed convection boundary layer flow from a horizontal circular cylinder in a nanofluid. *Int. J. Numer. Method H.* **2012**, *22*, 576–606. [CrossRef]
67. Rashad, A.; Chamkha, A.; Modather, M. Mixed convection boundary-layer flow past a horizontal circular cylinder embedded in a porous medium filled with a nanofluid under convective boundary condition. *Comput. Fluids* **2013**, *86*, 380–388. [CrossRef]
68. Hamarsheh, A.S.; Alwawi, F.A.; Alkasasbeh, H.T.; Rashad, A.M.; Idris, R. Heat transfer improvement in MHD natural convection flow of graphite oxide/carbon nanotubes-methanol based casson nanofluids past a horizontal circular cylinder. *Processes* **2020**, *8*, 1444. [CrossRef]
69. Hussanan, A.; Salleh, M.Z.; Alkasasbeh, H.T.; Khan, I. MHD flow and heat transfer in a Casson fluid over a nonlinearly stretching sheet with Newtonian heating. *Heat Transf. Res.* **2018**, *49*, 1185–1198. [CrossRef]
70. Pop, I.; Ingham, D.B. *Convective Heat Transfer: Mathematical and Computational Modelling of Viscous Fluids and Porous Media*; Elsevier: Amsterdam, The Netherlands, 2001.
71. Acheson, D.J. *Elementary Fluid Dynamics*; Acoustical Society of America, Oxford University Press Inc.: New York, NY, USA, 1991.
72. Manzoor, T.; Zafar, M.; Iqbal, S.; Nazar, K.; Ali, M.; Saleem, M.; Manzoor, S.; Kim, W.Y. Theoretical Analysis of Roll-Over-Web Surface Thin Layer Coating. *Coatings* **2020**, *10*, 691. [CrossRef]
73. Manzoor, T.; Nazar, K.; Zafar, M.; Iqbal, S.; Ali, M.; Kim, W.Y.; Saleem, M.; Manzoor, S. Analysis of a thin layer formation of third-grade fluid. *Coatings* **2019**, *9*, 741. [CrossRef]
74. Ahmed, S.E.; Mansour, M.; Hussein, A.K.; Mallikarjuna, B.; Almeshaal, M.A.; Kolsi, L. MHD mixed convection in an inclined cavity containing adiabatic obstacle and filled with Cu–water nanofluid in the presence of the heat generation and partial slip. *J. Therm. Anal. Calorim.* **2019**, *138*, 1443–1460. [CrossRef]
75. Dinarvand, S.; Hosseini, R.; Pop, I. Axisymmetric mixed convective stagnation-point flow of a nanofluid over a vertical permeable cylinder by Tiwari-Das nanofluid model. *Powder Technol.* **2017**, *311*, 147–156. [CrossRef]
76. Molla, M.; Hossain, M.; Taher, M. Magnetohydrodynamic natural convection flow on a sphere with uniform heat flux in presence of heat generation. *Acta Mech.* **2006**, *186*, 75–86. [CrossRef]
77. Keller, H.B.; Bramble, J. Numerical solutions of partial differential equations. *Mathematics* **1970**, *1*, 81–94.

78. Jones, E. An asymptotic outer solution applied to the Keller box method. *J. Comput. Phys.* **1981**, *40*, 411–429. [CrossRef]
79. Cebeci, T.; Bradshaw, P. *Physical and Computational Aspects of Convective Heat Transfer*; Springer Science & Business Media: New York, NY, USA, 2012.
80. Shafie, S.; Gul, A.; Khan, I. Molybdenum disulfide nanoparticles suspended in water-based nanofluids with mixed convection and flow inside a channel filled with saturated porous medium. *AIP Conf. Proc.* **2016**, *1775*, 030042.
81. Brown, S.; Stewartson, K. Laminar separation. *Annu. Rev. Fluid Mech.* **1969**, *1*, 45–72. [CrossRef]
82. Curle, N. Development and separation of a laminar boundary layer with an exponentially increasing pressure gradient. *Q. J. Mech. Appl. Math.* **1981**, *34*, 383–396. [CrossRef]
83. Pauley, L.L.; Moin, P.; Reynolds, W.C. The structure of two-dimensional separation. *J. Fluid Mech.* **1990**, *220*, 397–411. [CrossRef]
84. Miles, J.W. Boundary-layer separation on a sphere in a rotating flow. *J. Fluid Mech.* **1971**, *45*, 513–526. [CrossRef]